

# Cell-Free Massive MIMO with Radio Stripes for Indoor Wireless Energy Transfer

Onel L. A. López, *Member, IEEE*, Dileep Kumar, *Student Member, IEEE*,  
Richard Demo Souza, *Senior Member, IEEE*, Petar Popovski, *Fellow, IEEE*, Antti  
Tölli, *Senior Member, IEEE*, and Matti Latva-aho, *Senior Member, IEEE*

## Abstract

Radio frequency wireless energy transfer (WET) is a promising solution for powering autonomous Internet of Things (IoT) deployments. Recent works on WET have mainly focused on extremely low-power/cost IoT applications. However, trending technologies such as energy beamforming and waveform optimization, distributed and massive antenna systems, smart reflect arrays and reconfigurable metasurfaces, flexible energy transmitters, and mobile edge computing, may broaden WET applicability, and turn it plausible for powering more energy-hungry IoT devices. In this work, we specifically leverage energy beamforming for powering multiple user equipments (UEs) with stringent energy harvesting (EH) demands in an indoor cell-free massive multiple-input multiple-output system (mMIMO). Based on semi-definite programming (SDP), successive convex approximation (SCA), and maximum ratio transmission (MRT) techniques, we derive optimal and sub-optimal precoders aimed at minimizing the radio stripes' transmit power while exploiting information of the power transfer efficiency of the EH circuits at the UEs. Moreover, we propose an analytical framework to assess and control the electromagnetic field (EMF) radiation exposure in the considered indoor scenario. Numerical results show that i) the EMF radiation exposure can be more easily controlled at higher frequencies at the cost of a higher transmit power consumption, ii) training is not a very critical factor for the considered indoor system, iii) MRT/SCA-based precoders are particularly appealing when serving a small number of UEs, thus, specially suitable

Onel López, Dileep Kumar, Antti Tölli and Matti Latva-aho are with the Centre for Wireless Communications University of Oulu, Finland, e-mails: {Onel.AlcarazLopez, Dileep.Kumar, Antti.Tolli, Matti.Latva-aho}@oulu.fi.

Richard Demo Souza is with Federal University of Santa Catarina (UFSC), Florianópolis, Brazil, e-mail: richard.demo@ufsc.br.

Petar Popovski is with the Department of Electronic Systems, Aalborg University, 9220 Aalborg, Denmark, e-mail: petarp@es.aau.dk

This work is supported by Academy of Finland (Aka) (Grants n.307492, n.319059, n.318927 (6Genesis Flagship)), CNPq, Print CAPES-UFSC "Automation 4.0", and RNP/MCTIC (Grant 01245.010604/2020-14) 6G Mobile Communications Systems. The work of Petar Popovski has been partially supported by EU H2020 RISE-6G project.

for implementation in a time domain multiple access (TDMA) scheduling framework, and iv) TDMA is more efficient than spatial domain multiple access (SDMA) when serving a relatively small number of UEs. Results suggest that additional boosting performance strategies are needed to increase the overall system efficiency, thus making the technology viable in practice.

### Index Terms

cell-free massive MIMO, channel state information (CSI), EMF, energy beamforming, IoT, MRT, WET, radio stripes, SCA, SDMA, SDP, TDMA.

## I. INTRODUCTION

The expected massive number of “Internet of Things” (IoT) devices coming online over the next decade is conditioned on first solving critical challenges, specially in terms of efficient massive access, light communication protocols, and sustainable powering mechanisms. As for the latter, existing solutions that rely on wired powering are usually cost-prohibitive or infeasible for ubiquitous deployment. Meanwhile battery-powered solutions face other drawbacks [1]: i) limited lifetime, influenced by activity/usage, ii) frequent maintenance as different devices, and corresponding lifetimes, may coexist in the same environment, and iii) the battery waste processing problem. Therefore, alternative powering mechanisms and related technologies need to be developed in the coming years to realize the vision of a data-driven sustainable society, enabled by near-instant, secure, unlimited and green massive connectivity [1], [2].

Radio frequency (RF) wireless energy transfer (WET) (hereinafter just referred to as WET) constitutes an appealing technology to be further researched, developed and exploited for powering IoT deployments [1]–[4]. Different from energy harvesting (EH) solutions relying on other energy sources, WET allows: i) small-form factor, ii) native multi-user support, and iii) relatively long range energy coverage. However, the ultra-low end-to-end power transfer efficiency (PTE) of WET systems, together with strict regulations on the electromagnetic field (EMF) radiation, are critical factors that may limit WET feasibility in practice. By addressing these challenges, while exploiting further advancements on ultra-low-power integrated circuits, WET may emerge as a revolutionary technology that will finally cut the “*last wires*” (i.e., cables for energy recharging [3]) for a truly wireless and autonomous connectivity. In fact, IoT industry is already strongly betting on this promising technology, proof of which is the variety of emerging enterprises with

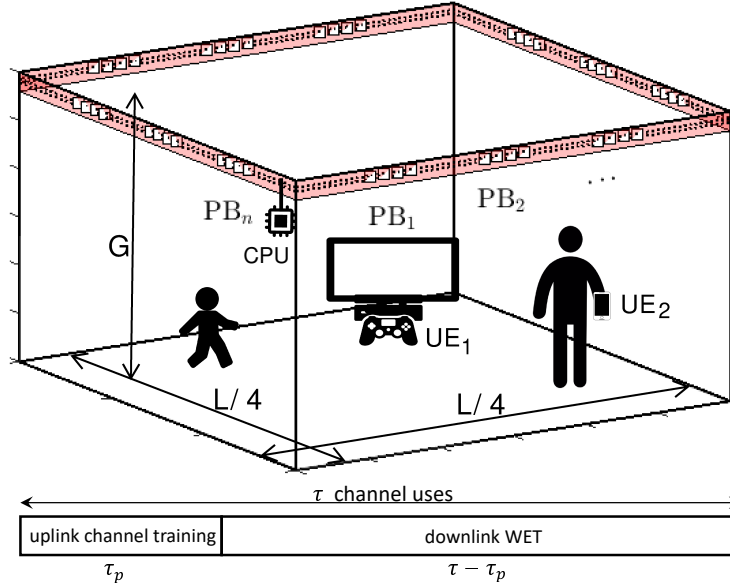


Fig. 1. System model with  $K = 2$ ,  $N = 12$  and  $M = 4$  (top), and structure of the training/charging protocol (bottom).

a large portfolio of WET solutions, for example Powercast, TransferFi and Ossia<sup>1</sup>.

Recent works on WET have mainly targeted extremely low-power/cost IoT applications, e.g., wireless sensor networks and RFIDs, because of the ultra-low PTE (see [1] and references therein). However, several promising technologies such as i) energy beamforming and waveform optimization [4]–[7], ii) distributed [8], [9] and massive antenna [9]–[15] systems, iii) smart reflect arrays and reconfigurable metasurfaces [16], iv) motor-equipped power beacons (PBs) [17], flying PBs [18], PBs with rotary antennas [7]), and v) mobile computation offloading and crowd sensing [4], may broaden WET applicability, and turn it plausible for powering more energy-hungry IoT devices, e.g., smartphones, game console controllers, electronic toys. In this work, we leverage some of above enablers to investigate WET's feasibility for power-hungry indoor charging. Specifically, optimal and sub-optimal energy beamforming schemes are proposed and discussed for a cell-free (distributed) massive multiple-input multiple-output (mMIMO) radio stripes system deployed in an indoor small-area environment (thus with limited serving distances) for multi-user RF wireless charging as illustrated in Fig. 1.

#### A. Related Work

The max-min throughput optimization problem for a mMIMO wireless powered communication network (WPCN) is addressed in [10]. Therein, authors show that the asymptotically,

<sup>1</sup>See <https://www.powercastco.com>, <https://www.transferfi.com> and <https://www.ossia.com>.

in the number of transmit antennas, optimal energy beamformer is akin to maximum ratio transmission (MRT) in MIMO communications. Taking advantage of the latter results, authors in [11] investigate the overall PTE and the energy efficiency (EE) of a wireless powered communication network (WPCN), where a mMIMO base station (BS) uses WET to charge single-antenna EH users in the downlink. A piece-wise linear EH model just considering sensitivity and saturation impairments is adopted, and it is shown that increasing the transmit power improves the EE as the number of antennas becomes large. However, authors in [10], [11] assume that all the harvested energy is used for uplink information transmission, ignoring other important energy consumption sources. Meanwhile, a low-complexity mMIMO WET scheme based on the retrodirective beamforming technique, where all EH devices send a common beacon simultaneously to the PB in the uplink and the PB simply conjugates and amplifies its received sum-signal for downlink WET, is investigated in [12] relying on the asymptotically optimum MRT-like precoding [10]. The performance in terms of received net energy (harvested energy minus energy consumed during training) of a multi-user mMIMO system with Rician fading channels is analyzed in [13]. Two different schemes are considered: i) training-based WET, and ii) line-of-sight (LOS) beamforming, and authors derive a user-specific path loss threshold for switching between them. The appeal of LOS-based beamforming is also illustrated in [7], where an MRT-based energy beamforming algorithm with low complexity for mMIMO is proposed. However, the system performance is analyzed only in the ultra-low EH regime in [7], [13], while the channel assumption in [13] is also very restrictive. Finally, readers may refer to [14], [15] where authors investigate the performance of mMIMO-enabled simultaneous wireless information and power transfer (SWIPT) systems.

As evinced above, single-transmitter mMIMO technology for WET has been considerably investigated. Surprisingly, much less efforts have been put to investigate distributed mMIMO technology, which makes WET more feasible by shortening the channel distances [9]. To the best of our knowledge, there is no prior work addressing cell-free mMIMO with radio stripes [19] for WET, in which actual PBs consist of antenna elements and circuit-mounted chips inside the protective casing of a cable/stripe, allowing imperceptible installation and alleviating the problem of deployment permissions [1]. We show later that it is indeed possible to deliver significant amounts of energy over practical third generation partnership project (3GPP) channels to multiple EH receivers by using this technology in an indoor small-area environment.

On the other hand, WET systems are subject to strict transmit constraints that limit their

performance in practice. Specifically, the EMF caused by energy radiation must be strictly limited in the presence of humans (and other living species) to reduce the risks of potential biological effects (e.g., tissue heating) [20], [21]. Concerns about adverse consequences of EMF exposure have resulted in the establishment of exposure limits<sup>2</sup> such as the maximum permissible exposure (MPE), also called power density, measured in  $[W/m^2]$ . Although several works have considered such important constraints in WET systems, e.g., [22], [23], to the best of our knowledge none has yet addressed them in the context of mMIMO WET, let alone in a distributed cell-free mMIMO setup for WET.

### *B. Contributions*

This article considers an indoor cell-free mMIMO system with radio stripes for multi-user WET under EMF-related constraints. Our main contributions are:

- 1) We introduce an indoor cell-free mMIMO system with radio stripes for wirelessly charging user equipments (UEs). The radio stripes system is composed of  $N > 1$  multi-antenna PBs subject to maximum transmit power constraints, which coherently beamform the energy signals towards the devices using channel state information (CSI) obtained from uplink training, and PTE information of the EH circuits at the UEs.
- 2) We formulate the semi-definite programming (SDP)-based precoding design that minimizes the transmit power subject to stringent EH requirements per user. Moreover, we apply the successive convex approximation (SCA) technique to reduce complexity, while a sub-optimal design based on MRT precoding is also proposed. For the special case of a single UE scenario, the MRT precoding is reformulated, and we show that it requires at most  $N$  low complexity iterative operations.
- 3) We propose an analytical framework to evaluate the RF power density in the proximity of the UEs, and that caused at a random point in the network. We formulate these figures in terms of EMF constraints and incorporate them to the original optimization problem accordingly.
- 4) We show that the spatial transmit gains from incorporating more PBs to the radio stripes at high frequencies do not compensate the path loss, demanding more transmit energy resources. However, the EMF radiation exposure can be more easily controlled at higher frequencies.

<sup>2</sup>EMF limits are set by the International Commission on Non-Ionizing Radiation Protection (ICNIRP) in most of Europe [20].

- 5) We provide numerical evidence that training is not a very critical (limiting) factor for the considered indoor (short-range) system as just little energy is required to attain a performance similar to that of a system with ideal CSI. Moreover, we show that the system incurs in a greater transmit power consumption once the per-PB power and EMF-related constraints are considered.
- 6) We discuss key trade-offs between spatial division multiple access (SDMA) and time division multiple access (TDMA). We show that TDMA is more efficient when serving a small number of UEs, while SDMA may be preferable when the number of UEs is large.

### C. Organization

The remainder of this paper is organized as follows. Section II introduces the system model and problem formulation. Sections III and IV present the global optimization framework, and alternative low-complexity solutions, respectively, while Section V addresses the single UE case. Section VI introduces the analytical framework for EMF-related metrics. Finally, Section VII presents numerical results, and Section VIII concludes the article.

*Notation:* Boldface lowercase/uppercase letters denote column vectors/matrices;  $\mathbf{1}$  is a vector of ones; while  $\mathbf{I}$  is the identity matrix. Superscripts  $(\cdot)^*$ ,  $(\cdot)^T$  and  $(\cdot)^H$  are the complex conjugate, transpose and Hermitian operations, respectively.  $\|\cdot\|$  and  $\text{Tr}(\cdot)$  are the Euclidean norm of a vector and trace of a matrix, respectively. The curled inequality symbol  $\succeq$  denotes generalized inequality: between vectors, it represents component-wise inequality; between symmetric matrices, it represents matrix inequality. Meanwhile,  $\mathbb{R}^+$  is the set of non-negative real numbers,  $\mathbb{S}^d$  is the set of Hermitian matrices of dimensions  $d \times d$ ,  $\mathbb{C}$  is the set of complex numbers, respectively, and  $\mathbf{j} = \sqrt{-1}$  is the imaginary unit. Additionally,  $\min\{\cdot\}$ ,  $\{\cdot\}$  and  $\lfloor \cdot \rfloor$  are the minimum, fractional part, and floor functions, respectively, while  $|\cdot|$  is the absolute (or cardinality for sets) operation.  $\mathbb{E}[\cdot]$  denotes statistical expectation,  $\Re\{\cdot\}$  outputs the real part of the argument, and  $\partial$  is partial differentiation. Finally,  $\mathcal{O}(\cdot)$  is the big-O notation, and  $\mathbf{x} \sim \mathcal{CN}(\bar{\mathbf{x}}, \mathbf{R})$  is a circularly-symmetric complex Gaussian random vector with mean  $\bar{\mathbf{x}}$  and covariance matrix  $\mathbf{R}$ .

## II. RADIO STRIPES SYSTEM MODEL

As in Fig. 1, we consider a cell-free mMIMO radio stripes network comprising of a set  $\mathcal{N}$  of  $|\mathcal{N}| = N$  PBs<sup>3</sup>, each with  $M$  antennas, wirelessly powering  $K \leq MN$  single antenna UEs in

<sup>3</sup>Although not relevant for the scenario discussed here, we may assume that front-haul connections goes from  $\text{PB}_1 \rightarrow \text{PB}_2 \rightarrow \text{PB}_3 \rightarrow \dots \rightarrow \text{PB}_N \rightarrow \text{central processing unit (CPU)}$ .

the downlink. In practice,  $K \ll MN$  should hold, and might be required so that the radio stripes system can energize relatively power hungry devices such as mobile phones, console controllers, etc. Such  $K$  UEs may have been scheduled in advance for the system to charge, thus may be part of a greater set of UEs with charging demands.

The PBs are equally placed on a radio stripe of length  $L$  (m) which is wrapped around a square perimeter of the same length, e.g., a room or office, at a height  $G$  from the floor level. Then, the number of PBs that can be deployed is upper bounded by

$$N < \frac{L}{M\lambda/2} = \frac{2L}{\lambda} \quad (1)$$

by considering half-wavelength spaced antenna elements, where  $\lambda$  is the system operation wavelength. Moreover, we consider quasi-static block Rician fading, such that the channel between  $\text{PB}_n$  and  $\text{UE}_k$  is distributed as

$$\mathbf{h}_{kn} \sim \mathcal{CN}(\bar{\mathbf{h}}_{kn}, \mathbf{R}_{kn}), \quad (2)$$

where  $\bar{\mathbf{h}}_{kn} \in \mathbb{C}^M$  is the LOS component and  $\mathbf{R}_{kn} \in \mathbb{C}^{M \times M}$  is the positive semi-definite covariance matrix. However, the methods and analysis presented in Sections III-V hold independently of the channel fading distribution. Further, the coherence block consists of  $\tau$  channel uses. Prior to the downlink WET, there is an uplink channel estimation phase consisting of  $\tau_p$  channel uses for pilots transmissions from the UEs. Therefore, the downlink WET occurs over the remaining  $\tau - \tau_p$  channel uses. Both phases are illustrated in Fig. 1 and described in the following.

#### A. Uplink Channel Estimation

We assume there are  $\tau_p$  mutually orthogonal  $\tau_p$ -length pilot vector signals  $\psi_1, \psi_2, \dots, \psi_{\tau_p}$ , with  $\|\psi_i\|^2 = \tau_p$ ,  $i = 1, \dots, \tau_p$ , which are used by the  $K$  UEs for channel estimation. We assume that  $K \leq \tau_p$  and the pilot sequence assigned to  $\text{UE}_k$  is  $\psi_k$ , thus, each UE owns a unique pilot sequence. Then, the pilot signal received at  $\text{PB}_n$  in the CSI acquisition phase is

$$\mathbf{Y}_n = \sum_{k=1}^K \sqrt{p_k} \mathbf{h}_{kn} \psi_k^T + \mathbf{W}_n, \quad (3)$$

where  $p_k \geq 0$  is the fixed transmit power of  $\text{UE}_k$ , and  $\mathbf{W}_n \in \mathbb{C}^{M \times \tau_p}$  is the noise at the receiver modeled with independent entries distributed as  $\mathcal{CN}(0, \sigma^2)$ .

Herein, we assume the least square (LS) channel estimate

$$\hat{\mathbf{h}}_{kn} = \frac{1}{\sqrt{p_k \tau_p}} \mathbf{Y}_n \psi_k^*, \quad (4)$$

where the channel error estimate  $\tilde{\mathbf{h}}_{kn}$  is distributed as

$$\tilde{\mathbf{h}}_{kn} = \frac{1}{\sqrt{p_k \tau_p}} \mathbf{W}_n \boldsymbol{\psi}_k^* \sim \mathcal{CN}\left(\mathbf{0}, \frac{\sigma^2}{p_k \tau_p} \mathbf{I}\right), \quad (5)$$

thus,  $\hat{\mathbf{h}}_{kn} \sim \mathcal{CN}(\bar{\mathbf{h}}_{kn}, \mathbf{R}_{kn} - \frac{\sigma^2}{p_k \tau_p} \mathbf{I})$ . Note that there is no need of using more complex methods such as the minimum mean square error (MMSE) estimator for this kind of short-distance setup. This is because pilots are orthogonal, and  $\frac{\sigma^2}{p_k \tau_p} \ll \mathbb{E}[\|\mathbf{h}_{kn}\|^2]$ , thus, channel estimates are already very precise when using LS. Moreover, the MMSE method would require prior knowledge of  $\bar{\mathbf{h}}_{kn}$  and  $\mathbf{R}_{kn}$ , which are subject to estimation errors that propagate to the actual estimate of  $\mathbf{h}_{kn}$  [24].

### B. Downlink WET

At each channel use of the downlink WET phase, each  $\text{PB}_n$  transmits  $K' \leq K$  energy symbols  $s_{k'} \in \mathbb{C}$  such that the RF signal received by  $\text{UE}_k$  is given by

$$y_k = \sum_{n=1}^N \sum_{k'=1}^{K'} \mathbf{v}_{k'n}^T \mathbf{h}_{kn} s_{k'}, \quad (6)$$

where  $\mathbf{v}_{k'n} \in \mathbb{C}^M$  is the precoding vector associated to  $s_{k'}$ . Note that, in general, the number of powering signals, thus, the number of precoders, does not necessarily need to match the number of UEs. However, as the energy requirements per UE become stringent, a dedicated beam per UE may be required. Moreover, noise impact is ignored since it is practically null for EH purposes, and it is assumed that symbols  $s_{k'}$  are independent random variables, i.e.,  $\mathbb{E}[s_k^* s_{k'}] = 0$ ,  $\forall k \neq k'$ , normalized so as to satisfy a unit average power constraint, i.e.,  $\mathbb{E}[\|s_{k'}\|^2] = 1$ . Then, the incident average RF power available at each  $\text{UE}_k$  per channel use of the WET phase is given by

$$\begin{aligned} P_k &= \mathbb{E}_s[\|y_k\|^2] = \mathbb{E}_s[y_k^* y_k] \stackrel{(a)}{=} \mathbb{E}_s \left[ \left( \sum_{k'_1=1}^{K'} \sum_{n_1=1}^N \mathbf{v}_{k'_1 n_1}^T \mathbf{h}_{kn_1} s_{k'_1} \right)^* \sum_{k'_2=1}^{K'} \sum_{n_2=1}^N \mathbf{v}_{k'_2 n_2}^T \mathbf{h}_{kn_2} s_{k'_2} \right] \\ &\stackrel{(b)}{=} \sum_{k'_1=1}^{K'} \sum_{k'_2=1}^{K'} \sum_{n_1=1}^N \sum_{n_2=1}^N \mathbf{v}_{k'_1 n_1}^H \mathbf{h}_{kn_1}^* \mathbf{v}_{k'_2 n_2}^T \mathbf{h}_{kn_2} \mathbb{E}_s[s_{k'_1}^* s_{k'_2}] \stackrel{(c)}{=} \sum_{k'=1}^{K'} \left| \sum_{n=1}^N \mathbf{v}_{k'n}^T \mathbf{h}_{kn} \right|^2, \end{aligned} \quad (7)$$

where (a) comes from using (6), (b) follows after re-arranging terms, and (c) is immediately attained from leveraging the assumption of independent and power-normalized signals. Meanwhile, the energy harvested by  $\text{UE}_k$  in a block (comprising both phases) converges to

$$E_k = \left(1 - \frac{\tau_p}{\tau}\right) g_k(P_k) \quad (8)$$

for sufficiently large  $\tau - \tau_p$ , e.g.,  $\tau - \tau_p \gg 10$ , and considering unit time blocks without loss of generality. Note that  $g_k : \mathbb{R}^+ \rightarrow 0 \cup [\varpi_k, \nu_k]$  is a non-decreasing function modeling the relation



between the incident RF power and harvested direct current (DC) power at UE<sub>k</sub>, and  $\varpi_k$  and  $\nu_k$  are the DC sensitivity and saturation levels, respectively. Although, in general,  $g_k$  also depends on the modulation and incoming waveform [25], we may ignore such effects if no optimization and/or different modulation schemes are utilized as is the case here.

### C. Problem Formulation

The goal is to minimize the power consumption of the radio stripes system by properly designing/setting the precoding vectors  $\{\mathbf{v}_{kn}\}$ .

The system is subject to per-PB power and per-UE EH constraints at each WET phase. This is, each PB circuit is subject to a total power constraint  $p_{\max}$ , and each UE<sub>k</sub> has a target energy requirement  $\xi_k$  per block. With a proper knowledge of devices EH hardware characteristics, i.e.,  $\{g_k\}$ , such constraint can be transformed to

$$\hat{E}_k \geq \xi_k \rightarrow \hat{P}_k \geq g_k^{-1}\left(\frac{\xi_k}{1 - \tau_p/\tau}\right) \triangleq \delta_k, \quad (9)$$

where the hat accent denotes estimation since the true channel realizations are never known with perfection, thus  $\hat{E}_k$  and  $\hat{P}_k$  can be evaluated using (8) and (7), respectively, but substituting  $\mathbf{h}_{kn}$  by  $\hat{\mathbf{h}}_{kn}$ . In practice, a constraint in the form of (9) does not prevent that the true harvested energy may fall below the threshold  $\delta_k$  for poorly estimated channel realizations. However, as we shall see later in Section VII, channel estimates are indeed very accurate in the considered setup. Moreover, small fluctuations around  $\delta_k$  average out when considering consecutive coherence time intervals and will not impact the WET performance in practice.

Since  $g_k$  is a non-decreasing function, it is invertible as long as  $\frac{\xi_k}{1 - \tau_p/\tau} < \nu_k$ .<sup>4</sup> Therefore, the optimization problem can be formulated as

$$\mathbf{P1} : \quad \underset{\mathbf{v}_{k'n} \in \mathbb{C}^M, \forall k', n}{\text{minimize}} \quad P_T = \sum_{n=1}^N \sum_{k'=1}^{K'} \|\mathbf{v}_{k'n}\|^2 \quad (10a)$$

$$\text{subject to} \quad \hat{P}_k(\{\mathbf{v}_{k'n}\}) \geq \delta_k, \quad \forall k, \quad (10b)$$

$$\sum_{k'=1}^{K'} \|\mathbf{v}_{k'n}\|^2 \leq p_{\max}, \quad \forall n, \quad (10c)$$

which is non-convex due to (10b). In Sections III-V we discuss different optimization approaches to solve P1. Meanwhile, note that the radio stripes deployment topology enables a distributed

<sup>4</sup>Obviously  $\frac{\xi_k}{1 - \tau_p/\tau} > \nu_k$  is not practically viable; while in case  $\frac{\xi_k}{1 - \tau_p/\tau} = \nu_k$ , we can set  $g_k^{-1}(\nu_k)$  to be  $\lim_{x \rightarrow \nu_k^-} g_k^{-1}(x)$ .

3D beamforming (avoiding the generation of strong beams since transmit antenna elements are spread over a square perimeter) pointing to the locations of the UEs, where the EMF exposure levels are expected to be the greatest. However, **P1**, in its current form, does not prevent increased EMF levels at other spatial points as well. A EMF-aware optimization, under which EMF-related constraints are incorporated into **P1**, is addressed later in Section VI.

### III. GLOBAL OPTIMIZATION FRAMEWORK

Let us proceed by defining

$$\mathbf{v}_k = [\mathbf{v}_{k1}^T, \mathbf{v}_{k2}^T, \dots, \mathbf{v}_{kN}^T]^T, \quad (11)$$

$$\hat{\mathbf{h}}_k = [\hat{\mathbf{h}}_{k1}^T, \hat{\mathbf{h}}_{k2}^T, \dots, \hat{\mathbf{h}}_{kN}^T]^T. \quad (12)$$

Then, departing from (7) we have that

$$\begin{aligned} \hat{P}_k &= \sum_{k'=1}^{K'} \left| \sum_{n=1}^N \mathbf{v}_{k'n}^T \hat{\mathbf{h}}_{kn} \right|^2 = \sum_{k'=1}^{K'} |\mathbf{v}_{k'}^T \hat{\mathbf{h}}_k|^2 = \sum_{k'=1}^{K'} (\mathbf{v}_{k'}^T \hat{\mathbf{h}}_k)^H (\mathbf{v}_{k'}^T \hat{\mathbf{h}}_k) = \sum_{k'=1}^{K'} \hat{\mathbf{h}}_k^H \mathbf{v}_{k'}^* \mathbf{v}_{k'}^T \hat{\mathbf{h}}_k \\ &= \hat{\mathbf{h}}_k^H \left[ \sum_{k'=1}^{K'} (\mathbf{v}_{k'} \mathbf{v}_{k'}^H)^T \right] \hat{\mathbf{h}}_k = \text{Tr}(\mathbf{V}^T \hat{\mathbf{H}}_k), \end{aligned} \quad (13)$$

where  $\mathbf{V} = \sum_{k'=1}^{K'} \mathbf{v}_{k'} \mathbf{v}_{k'}^H$  and  $\hat{\mathbf{H}}_k = \hat{\mathbf{h}}_k \hat{\mathbf{h}}_k^H$ . Now,  $\mathbf{V}$  can be optimally found by solving the following (convex) SDP

$$\mathbf{P2}: \quad \underset{\mathbf{V} \in \mathbb{S}^{MN}}{\text{minimize}} \quad P_T = \text{Tr}(\mathbf{V}) \quad (14a)$$

$$\text{subject to} \quad \text{Tr}(\mathbf{V}^T \hat{\mathbf{H}}_k) \geq \delta_k, \quad \forall k, \quad (14b)$$

$$\mathbf{B} \text{diag}(\mathbf{V}) \preceq p_{\max} \mathbf{1}, \quad (14c)$$

$$\mathbf{V} \succeq \mathbf{0}, \quad (14d)$$

where  $\mathbf{B} \in \{0, 1\}^{N \times NM}$  is a sensing matrix designed to collect the total transmit power of each PB, thus, it has unit entries from the  $(i(M-1)+1)$ -th until the  $iM$ -th element of each row  $i = 1, \dots, N$ , and zero in the remaining entries. Notice that (14a), (14b) and (14c) are equivalent to (10a), (10b) and (10c), respectively. After solving **P2** using standard convex optimization frameworks, e.g., CVX [26], the composite precoding vectors  $\{\mathbf{v}_{k'}\}$ , with  $K'$  equal to the rank of  $\mathbf{V}$ , can be obtained as the eigenvectors of  $\mathbf{V}$ .

Interestingly, the precoding optimization for information multicasting, where the same information-bearing signal is simultaneously transmitted to all users, usually relies on a semi-definite relaxation with a structure similar to that of (14) [27]. Therefore, after solving the SDP, it requires a

last step to force rank-1 multicast beamforming, e.g., via Gaussian randomization, thus leading to sub-optimal solutions. Meanwhile, the optimum energy precoding here is not rank constrained since energy can be collected from any arbitrary superposition of energy carrying symbols, thus, directly obtained from solving **P2**.

#### A. Problem Feasibility

Note that by removing the per-PB power constraint (14c) from **P2**, the resulting relaxed problem is always feasible. This is because for any precoding phase design, the corresponding transmit power could boundlessly increase until constraints in (14b) are met. Therefore, the problem feasibility can be verified by i) finding the minimum  $p_{\max}$  that allows satisfying (14b)–(14d), and ii) verifying that it is indeed not greater than the physical per-PB power constraint. Note that the feasibility may be controlled by the charging scheduling decision, which establishes the set of UEs to be served, thus regulating the influence of constraint (14b).

#### B. Complexity Analysis

Interior point methods are usually adopted to efficiently find the optimal solution of SDP formulations. In this case, it can be shown that solving **P2** requires around  $\mathcal{O}(\sqrt{MN} \log(1/\epsilon))$  iterations, with each iteration requiring  $\mathcal{O}(M^6 N^6 + (K+N)MN)$  arithmetic operations [28], and where  $\epsilon$  represents the solution accuracy attained when the algorithm ends. Consequently, both, determining the problem feasibility and finding the optimum solution, become computationally costly as the total number of antenna elements of the radio stripes system increases. To achieve complexity reduction, a low-complexity optimization approach is proposed next as an efficient alternative to attain near-optimum performance.

### IV. LOW-COMPLEXITY OPTIMIZATION

In this section, we elaborate on finding a low-complexity solution for the original non-convex problem **P1**. We adopt the SCA technique [29], [30], wherein the non-convex problem is recast as a sequence of convex subproblems, and then iteratively solved until convergence.

#### A. Optimal Precoder Design

First, let us rewrite  $\hat{P}_k$  as

$$\hat{P}_k = \sum_{k'=1}^K \mathbf{v}_{k'}^H \mathbf{H}_k^T \mathbf{v}_{k'}, \quad (15)$$

which comes from a procedure similar to that leading to (13). Now, observe that constraint (10b) can be written as  $\delta_k - \hat{P}_k \leq 0$ ,  $\forall k$ , where  $\hat{P}_k$  is quadratic, thus a convex function [31, Ch. 3]. Therefore, the rewritten constraint constitutes a difference of convex functions, thus its best convex approximation can be obtained by replacing  $\hat{P}_k$  with its first-order approximation [30]. The first-order Taylor approximation of  $\hat{P}_k$  around a fixed operating point  $\{\bar{\mathbf{v}}_{k'}\}$  can be expressed as

$$\tilde{\hat{P}}_k \triangleq \sum_{k'=1}^K \bar{\mathbf{v}}_{k'}^H \mathbf{H}_k^T \bar{\mathbf{v}}_{k'} + 2 \sum_{k'=1}^K \Re\{\bar{\mathbf{v}}_{k'}^H \hat{\mathbf{H}}_k^T (\mathbf{v}_{k'} - \bar{\mathbf{v}}_{k'})\} = 2 \sum_{k'=1}^K \Re\{\bar{\mathbf{v}}_{k'}^H \hat{\mathbf{H}}_k^T \mathbf{v}_{k'}\} - \text{Tr}(\bar{\mathbf{V}}^T \hat{\mathbf{H}}_k), \quad (16)$$

where  $\bar{\mathbf{V}} = \sum_{k=1}^K \bar{\mathbf{v}}_k \bar{\mathbf{v}}_k^H$ . Hence, **P1** can be approximated in the vicinity of a fixed operating point  $\{\bar{\mathbf{v}}_{k'n}\}$  as

$$\mathbf{P3} : \quad \underset{\mathbf{v}_{k'n} \in \mathbb{C}^M, \forall k', n}{\text{minimize}} \quad P_T = \sum_{n=1}^N \sum_{k'=1}^{K'} \|\mathbf{v}_{k'n}\|^2 \quad (17a)$$

$$\text{subject to} \quad \tilde{\hat{P}}_k(\{\mathbf{v}_{k'}\}, \{\bar{\mathbf{v}}_{k'}\}) \geq \delta_k, \quad \forall k, \quad (17b)$$

$$\sum_{k'=1}^{K'} \|\mathbf{v}_{k'n}\|^2 \leq p_{\max}, \quad \forall n. \quad (17c)$$

Thus, by iteratively solving problem **P3** while updating  $\{\bar{\mathbf{v}}_{k'n}\}$  with the solution at each iteration, we can find the best local optimal solution [30]. The proposed low-complexity iterative method for problem **P1** is summarized in Algorithm 1.

### B. MRT based Precoder Design

In this subsection, we exploit further complexity reduction by adopting an approach similar to the proposed in [7], [10]–[12]. The key lies in setting  $K' = K$  and adopting a precoder design akin to MRT in MIMO communications as follows

$$\mathbf{v}_{kn} = \frac{\hat{\mathbf{h}}_{kn}^*}{\|\hat{\mathbf{h}}_{kn}\|} \sqrt{p_{kn}}, \quad \forall k, n, \quad (18)$$

where  $p_{kn}$  represents the power budget of  $\text{PB}_n$  for  $s_k$ . Then, with perfect CSI knowledge, the  $k$ -th signal transmitted from all radio stripes antennas arrives at  $\text{UE}_k$  with constructive superposition. Meanwhile, note that the impact of the signals meant to other devices on the energy harvested at  $\text{UE}_k$  is not considered for the phases' design, thus leading to an unavoidable performance degradation with respect to the SDP-based and/or SCA-based optimal solution previously discussed. With above precoder, the estimated RF incident power available at each  $\text{UE}_k$  per channel use of a WET phase given in (7) transforms to

$$\hat{P}_k = \sum_{k'=1}^K \left| \sum_{n=1}^N \sqrt{p_{k'n}} \frac{\hat{\mathbf{h}}_{k'n}^H}{\|\hat{\mathbf{h}}_{k'n}\|} \hat{\mathbf{h}}_{kn} \right|^2 = \sum_{k'=1}^K \left| \sum_{n=1}^N \varrho_{k'n} \mathbf{q}_{k'n}^H \hat{\mathbf{h}}_{kn} \right|^2 \quad (19)$$

---

**Algorithm 1** SCA-based Optimum Precoder
 

---

- 1: **Input:**  $\{\hat{\mathbf{h}}_{kn}\}, \delta_k, p_{\max} \quad \forall k \in \mathcal{K}, \forall n \in \mathcal{N}$
  - 2: Initialize  $\{\bar{\mathbf{v}}_{k'n}\}, \forall k' \in \mathcal{K}, \forall n \in \mathcal{N}$
  - 3: **repeat**
  - 4:   Solve problem **P3** with  $\{\bar{\mathbf{v}}_{k'n}\}$  and denote the local solution as  $\{\mathbf{v}_{k'n}^*\}$
  - 5:   Update  $\{\bar{\mathbf{v}}_{k'n}\} \leftarrow \{\mathbf{v}_{k'n}^*\}, \forall k \in \mathcal{K}, \forall n \in \mathcal{N}$
  - 6: **until** convergence or fixed number of iterations
  - 7: **Output:**  $\{\mathbf{v}_{k'n}^{\text{opt}}\}, \forall k \in \mathcal{K}, \forall n \in \mathcal{N}$
- 

where  $\varrho_{k'n} \triangleq \sqrt{p_{k'n}}$  becomes now the optimization variable, and  $\mathbf{q}_{k'n} \triangleq \hat{\mathbf{h}}_{k'n}/\|\hat{\mathbf{h}}_{k'n}\|$  denotes the normalized precoder.

We can observe that by using expression (19) in problem **P1**, the constraint (10b) is a difference of convex functions, and hence **P1** is still non-convex problem. We again resort to SCA framework [30] to find a solution. The first-order Taylor approximation of  $\hat{P}_k$  around a fixed operating point  $\{\bar{\varrho}_{k'n}\}$  can be expressed as

$$\tilde{P} \triangleq \sum_{k'=1}^{K'} \left| \sum_{n=1}^N \bar{\varrho}_{k'n} \mathbf{q}_{k'n}^H \mathbf{h}_{kn} \right|^2 + 2 \sum_{k'=1}^K \Re \left\{ \sum_{n=1}^N \bar{\varrho}_{k'n} \mathbf{h}_{kn}^H \mathbf{q}_{k'n} \left( \sum_{n=1}^N (\varrho_{k'n} - \bar{\varrho}_{k'n}) \mathbf{q}_{k'n}^H \mathbf{h}_{kn} \right) \right\}. \quad (20)$$

Hence, by using (20), the MRT-optimum precoder can be found by solving

$$\mathbf{P4} : \quad \underset{\varrho_{kn} \in \mathbb{R}^+, \forall k, n}{\text{minimize}} \quad P_T = \sum_{n=1}^N \sum_{k=1}^K \varrho_{kn}^2 \quad (21a)$$

$$\text{subject to} \quad \tilde{P}(\{\varrho_{k'n}\}, \{\bar{\varrho}_{k'n}\}) \geq \delta_k, \quad \forall k, \quad (21b)$$

$$\sum_{k=1}^K \varrho_{kn}^2 \leq p_{\max}, \quad \forall n, \quad (21c)$$

where the fixed operating point  $\{\bar{\varrho}_{k'n}\}$  is iteratively updated as summarized in Algorithm 2.

### C. Complexity Analysis

The approximated convex problems **P3** and **P4** can be efficiently solved using generic convex optimization tools, i.e., as a sequence of second-order cone program (SOCP) [31]. Interior points methods are usually adopted to efficiently solve SOCP formulations, and would require a number of iterations in the order of  $\mathcal{O}(\sqrt{MN} \log(1/\epsilon))$  and  $\mathcal{O}(\sqrt{N} \log(1/\epsilon))$  in case of **P3** and **P4**, respectively. Note that in case of **P3**, such required number of iterations matches that of the SDP formulation in **P2**. Meanwhile, **P4** does require less iterations, but such gain may disappear once the SCA iterative procedure of Algorithm 2, by which **P4** needs to be repeatedly solved, is taken into account. However, the clear and definite advantage behind using the optimization methods proposed in this section lies on the significantly reduced worst-case computational requirement

---

**Algorithm 2** MRT-based Precoder
 

---

- 1: **Input:**  $\{\hat{\mathbf{h}}_{kn}\}, \delta_k, p_{\max} \forall k \in \mathcal{K}, \forall n \in \mathcal{N}$
  - 2: Set  $i = 1$  and initialize  $\bar{\varrho}_{k'n} \forall k' \in \mathcal{K}, \forall n \in \mathcal{N}$
  - 3: **repeat**
  - 4:   Solve problem **P4** with  $\{\bar{\varrho}_{k'n}\}$  and denote the local solution as  $\{\varrho_{k'n}^*\}$
  - 5:   Update  $\{\bar{\varrho}_{k'n}\} \leftarrow \{\varrho_{k'n}^*\}, \forall k \in \mathcal{K}, \forall n \in \mathcal{N}$
  - 6:   Set  $i = i + 1$
  - 7: **until** convergence or fixed number of iterations
  - 8: **Output:**  $\{\varrho_{k'n}^{\text{opt}}\}, \forall k \in \mathcal{K}, \forall n \in \mathcal{N}$
- 

of each SCA iteration. Note that solving **P3** requires  $\mathcal{O}(M^3 N^3 + (K + N)MN)$  arithmetic operations, while **P4** is solvable using  $\mathcal{O}(MN + (K + N)MN)$  arithmetic operations.

## V. SINGLE UE CASE

Herein, we study a scenario of particular interest: the single UE case. Note that the system may serve the UEs in a TDMA fashion, in which case the derivations and performance analysis here hold accurate. Alternatively, the performance results for this scenario correspond to upper bounds of what it is expected if more UEs are simultaneously served in the same time interval.

### A. Optimum Precoder

In case of a single UE, the MRT-like precoder discussed in Section IV-B is the optimum. Then, let us relax the per-PB power constraint. The optimum concatenated precoder is

$$\mathbf{v}_1 = \frac{\hat{\mathbf{h}}_1^*}{\|\hat{\mathbf{h}}_1\|} \sqrt{p}, \quad (22)$$

where  $\mathbf{v}_1$  and  $\mathbf{h}_1$  obey (11) and (12), respectively. Then, we have that

$$\hat{P}_1 = |\mathbf{v}_1^T \hat{\mathbf{h}}_1|^2 = p \|\hat{\mathbf{h}}_1\|^2, \quad (23)$$

thus  $p^{\text{opt}} = \delta_1 / \|\hat{\mathbf{h}}_1\|^2$ . However, such solution may demand a transmit power above the per-PB power constraint  $p_{\max}$  at some PB since  $p_{1n}$  would need to be

$$p_{1n} = \|\mathbf{v}_{1n}\|^2 = \frac{p \|\hat{\mathbf{h}}_{1n}\|^2}{\|\hat{\mathbf{h}}_1\|^2} \quad (24)$$

and has not been bounded.

Let us assume that the set  $\mathcal{N}' \subseteq \mathcal{N}$  of PBs operating with transmit power below  $p_{\max}$  is known beforehand. Then, we have that

$$\hat{P}_1 = \left( \sqrt{p_{\max}} \sum_{n \in \mathcal{N}' \setminus \mathcal{N}} \|\hat{\mathbf{h}}_{1n}\| + \sum_{n \in \mathcal{N}'} \varrho_n \|\hat{\mathbf{h}}_{1n}\| \right)^2 \geq \delta_1 \rightarrow \underbrace{\sum_{n \in \mathcal{N}'} \varrho_n \|\hat{\mathbf{h}}_{1n}\|}_{\sqrt{\delta_1'}} \geq \sqrt{\delta_1} - \sqrt{p_{\max}} \sum_{n \in \mathcal{N}' \setminus \mathcal{N}} \|\hat{\mathbf{h}}_{1n}\|, \quad (25)$$

where  $\varrho_n \triangleq \sqrt{p_{1n}}$ . Using this result, one can transform **P1** to obtain

$$\mathbf{P5}: \underset{\varrho_n \in \mathbb{R}^+, \forall n}{\text{minimize}} \quad P_T = \sum_{n \in \mathcal{N}'} \varrho_n^2 \quad (26a)$$

$$\text{subject to} \quad \hat{P}_1' = \sum_{n \in \mathcal{N}'} \varrho_n \|\hat{\mathbf{h}}_{1n}\| \geq \sqrt{\delta_1'}. \quad (26b)$$

Now, let us write the Lagrangian of **P5** as

$$\mathcal{L}(\varrho_n, \mu) = \sum_{n \in \mathcal{N}'} \varrho_n^2 + \left( \sqrt{\delta_1'} - \sum_{n \in \mathcal{N}'} \varrho_n \|\hat{\mathbf{h}}_{1n}\| \right) \mu, \quad (27)$$

where  $\mu \geq 0$  is the Lagrangian multiplier. Observe that (27) is a convex quadratic function of every  $\varrho_n$ , thus minimized at

$$\frac{\partial \mathcal{L}(\varrho_n, \mu)}{\partial \varrho_n} = 2\varrho_n - \mu \|\hat{\mathbf{h}}_{1n}\| = 0 \quad \rightarrow \quad \varrho_n^{\text{opt}} = \frac{\mu}{2} \|\hat{\mathbf{h}}_{1n}\|. \quad (28)$$

Then, the Lagrange dual of **P5** is given by

$$\mathbf{P6}: \underset{\mu \geq 0}{\text{maximize}} \quad \mathcal{L}(\varrho_n^{\text{opt}}, \mu) = \mu \sqrt{\delta_1'} - \frac{\mu^2}{4} \sum_{n \in \mathcal{N}'} \|\hat{\mathbf{h}}_{1n}\|^2, \quad (29a)$$

for which

$$\mu^{\text{opt}} = \frac{2\sqrt{\delta_1'}}{\sum_{n \in \mathcal{N}'} \|\hat{\mathbf{h}}_{1n}\|^2}. \quad (30)$$

Therefore, substituting (30) into (28) yields the optimum solution of **P5**, which is given by

$$\varrho_n^{\text{opt}} = \frac{\|\hat{\mathbf{h}}_{1n}\| \sqrt{\delta_1'}}{\sum_{n \in \mathcal{N}'} \|\hat{\mathbf{h}}_{1n}\|^2}. \quad (31)$$

This means that if the set  $\mathcal{N} \setminus \mathcal{N}'$  of PBs are known to operate with transmit power  $p_{\max}$ , the remaining PBs optimum transmit power is given by  $p_{1n}^{\text{opt}} = (\varrho_n^{\text{opt}})^2$ , where  $\varrho^{\text{opt}}$  is given in (31).

Finally, the optimum precoder can be constructed as shown in Algorithm 3. In a nutshell, the transmit power of each PB is computed by exploiting (31) (line 8). In case a power allocation exceeds the maximum allowed power  $p_{\max}$ , it is immediately reduced to match  $p_{\max}$  (lines 4-6). The process is repeated until all PBs are allocated a transmit power not greater than  $p_{\max}$ . Note that this is an extremely simple optimization algorithm, where at most  $N$  iterative computations of (31) are required, but still provides the optimum WET precoder.

### B. Problem Feasibility

The feasibility of a single UE optimization problem is rather simple to verify. It is enough setting  $p_{1n} = p_{\max}, \forall n \in \mathcal{N}$ , and determine whether  $\hat{P}_1 \geq \delta_1$  holds or not. In this case,  $\hat{P}_1$  can

---

**Algorithm 3** Single-UE Optimum Precoder
 

---

- 1: **Input:**  $\{\hat{\mathbf{h}}_{1n}\}_{n \in \mathcal{N}}, \delta_1, p_{\max}$
  - 2: Set  $\mathcal{N}' = \mathcal{N}, p_{1n} = 0, \forall n \in \mathcal{N}$
  - 3: **repeat**
  - 4:   Set  $\mathcal{N}'' = \{n \in \mathcal{N}' | p_{1n} \geq p_{\max}\}$
  - 5:   Update  $p_{1n} \leftarrow p_{\max}, \forall n \in \mathcal{N}''$
  - 6:   Update  $\mathcal{N}' \leftarrow \mathcal{N}' \setminus \mathcal{N}''$
  - 7:   Update  $\delta'_1$  according to (25)
  - 8:   Set  $p_{1n} = (\varrho_n^{\text{opt}})^2, \forall n \in \mathcal{N}',$  according to (31)
  - 9: **until**  $p_{1n} \leq p_{\max}, \forall n \in \mathcal{N}$
  - 10: **Output:**  $p_{1n}^{\text{opt}} \leftarrow p_{1n}, \forall n \in \mathcal{N}$
- 

be evaluated departing from (19) as

$$\hat{P}_1 = \left( \sum_{n=1}^N \sqrt{p_{\max}} \|\hat{\mathbf{h}}_{1n}\| \right)^2 = p_{\max} \left( \sum_{n=1}^N \|\hat{\mathbf{h}}_{1n}\| \right)^2. \quad (32)$$

Then, if  $\sum_{n=1}^N \|\hat{\mathbf{h}}_{1n}\| \geq \sqrt{\delta_1/p_{\max}}$ , we can conclude the problem is feasible and the solution can be obtained from Algorithm 3. Finally, note that in the scenario with  $K > 1$  UEs it is sufficient (but not necessary) that  $\sum_{n=1}^N \|\hat{\mathbf{h}}_{kn}\| < \sqrt{\delta_k/p_{\max}}$  for some  $k$  to declare that P4 is not feasible.

### C. Minimum Average Radio Stripes Transmit Power

One interesting question is how much average power is required to serve the UE. The minimum average transmit power required by the radio stripes system can be computed by assuming no per-PB power constraint as follows

$$\mathbf{E}[P_T] = \mathbf{E}[\delta_1/|\hat{\mathbf{h}}_1|^2] \stackrel{(a)}{\geq} \delta_1/\mathbf{E}[|\hat{\mathbf{h}}_1|^2] = \delta_1/\sum_{n=1}^N \text{Tr}(\mathbf{R}_{1n}), \quad (33)$$

where (a) comes from applying Jensen's inequality.

## VI. EMF-AWARE OPTIMIZATION

In this section, we present an analytical framework to determine, analyze and limit EMF exposure levels. Different from previous sections where results are generic, herein we rely on the assumption of quasi-static Rician fading. However, the accuracy of our approaches and claims here should still approximately hold when considering other (more practical) fading distributions with the same first and second order statistics, i.e, same  $\bar{\mathbf{h}}_{kn}$  and  $\mathbf{R}_{kn}$ . The latter is because the channel hardening and favorable propagation phenomena enabled by mMIMO, which makes the communication performance almost independent of the small-scale fading realizations [32].



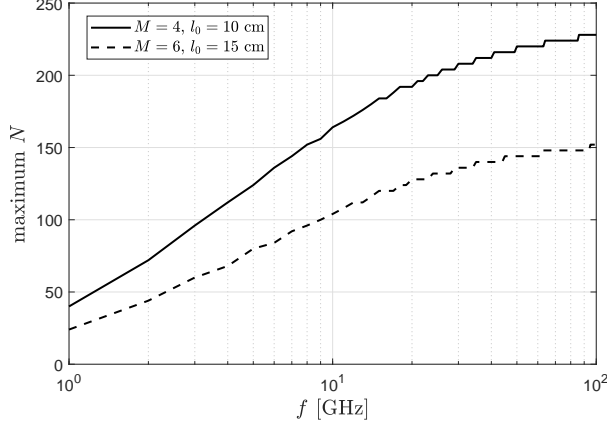


Fig. 2. Maximum number of PBs that can fit in the radio stripes system as a function of  $f$ . We set  $L = 24$  m.

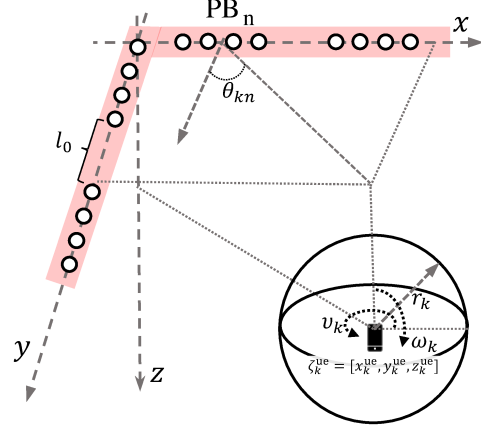


Fig. 3. Illustration of the geometry of the scenario.

We assume each PB of the radio stripes (Fig. 1) is equipped with a relative small number of antennas such that  $p_{\max}M$  is bounded to a desired level<sup>5</sup>, and we impose a separation restriction  $l_0 > \lambda/2$  between consecutive PBs. To ease the deployment and system design, we assume that no PB expands over any consecutive two sides of the perimeter, thus, the upper bound in (1) further tightens to

$$N \leq 4 \left\lfloor \frac{L/4}{(M-1)\lambda/2 + l_0} \right\rfloor = 4 \left\lfloor \frac{L}{2(M-1)\lambda + 4l_0} \right\rfloor. \quad (34)$$

As an example, Fig. 2 illustrates the maximum number of PBs that could be equipped in the radio stripes system as a function of the central operation frequency  $f$ .

Note that the focus of our work is on indoor scenarios where LOS channels are predominant. Thus, we first characterize the LOS channels and then introduce the EMF exposure metrics.

#### A. LOS Geometry

The geometry of the discussed scenario is illustrated in Fig. 3. The LOS (geometric) channel component between  $PB_n$  and  $UE_k$  is given by

$$\bar{\mathbf{h}}_{kn} = \sqrt{\beta_{kn}^{\text{los}}} e^{j(\varphi_{kn} \mathbf{1} + \Phi_{kn})}, \quad (35)$$

where  $\beta_{kn}^{\text{los}}$  denotes its large-scale fading component. Herein we adopt the following 3GPP indoor LOS path-loss model [33]

$$\beta_{kn}^{\text{los}} = -17.3 \log_{10} d(\zeta_n^{\text{ap}}, \zeta_k^{\text{ue}}) - 20 \log_{10} f - 32.4 \text{ [dB]}, \quad (36)$$

where  $\zeta_n^{\text{ap}} = [x_n^{\text{ap}}, y_n^{\text{ap}}, z_n^{\text{ap}}]^T$  and  $\zeta_k^{\text{ue}} = [x_k^{\text{ue}}, y_k^{\text{ue}}, z_k^{\text{ue}}]^T$  are the 3D coordinate position of the  $PB_n$ 's antenna array and  $UE_k$ ,  $f$  is given in GHz, and distance  $d(\zeta_1, \zeta_2) = \|\zeta_1 - \zeta_2\|$  is measured in

<sup>5</sup>Assuming a small number of antennas per PB also implies that each UE is in the far field with respect to all PBs.

meters. Note that the non-LOS (NLOS) channel component  $\mathbf{h}_{kn}^{\text{nlos}}$ , such that  $\mathbf{h}_{kn} = \bar{\mathbf{h}}_{kn} + \mathbf{h}_{kn}^{\text{nlos}}$ , would be distributed as  $\mathbf{h}_{kn}^{\text{nlos}} \sim \mathcal{CN}(\mathbf{0}, \mathbf{R}_{kn} - \bar{\mathbf{h}}_{kn}\bar{\mathbf{h}}_{kn}^H)$ , where

$$\text{Tr}(\mathbf{R}_{kn} - \bar{\mathbf{h}}_{kn}\bar{\mathbf{h}}_{kn}^H) = M\beta_{kn}^{\text{nlos}} \rightarrow \text{Tr}(\mathbf{R}_{kn}) = M(\beta_{kn}^{\text{los}} + \beta_{kn}^{\text{nlos}}) \quad (37)$$

with [33]

$$\beta_{kn}^{\text{nlos}} = \min \{ \beta_{kn}^{\text{los}} [\text{dB}], -38.3 \log_{10} d(\zeta_n^{\text{ap}}, \zeta_k^{\text{ue}}) - 24.9 \log_{10} f - 17.30 \} [\text{dB}]. \quad (38)$$

Moreover, the Rician LOS factor as a measure of how strong the LOS channel is with respect to the NLOS components is thus defined as  $\kappa_{kn} = \beta_{kn}^{\text{los}} / \beta_{kn}^{\text{nlos}}$ , and  $\kappa_{kn} > 0$  dB holds.

Meanwhile, the  $i$ -th entry of  $\Phi_{kn}$  in (35) corresponds to the mean phase shift between the  $i$ -th and the first array element of  $\text{PB}_n$ , thus, we have [34, Ch. 5]

$$\Phi_{kn} = -[0, 1, \dots, M-1]^T \pi \sin \theta_{kn}, \quad (39)$$

where  $\theta_{kn}$  is the azimuth angle relative to the boresight of the  $\text{PB}_n$ 's antenna array, thus

$$\sin \theta_{kn} = \frac{|\zeta_n^{\text{ap}} - \zeta_k^{\text{ue}}|}{d_{xy}(\zeta_n^{\text{ap}}, \zeta_k^{\text{ue}})}, \quad (40)$$

where  $\varsigma = x$  or  $\varsigma = y$  if the antenna array of the corresponding PB is aligned with the  $x$  or  $y$  axis, respectively, while  $d_{xy}(\zeta_1, \zeta_2) = \sqrt{(x_1 - x_2)^2 + (y_1 - y_2)^2}$  is the  $x-y$  distance component between  $\zeta_1$  and  $\zeta_2$ . Finally,  $\varphi_{kn}$  accounts for an initial phase shift, which in our case depends on the PB and UE position as

$$\varphi_{kn} = 2\pi \left\{ \frac{1}{\lambda} \|\zeta_1 - \zeta_2\| \right\}. \quad (41)$$

### B. EMF Level in the Proximity of the UEs

Herein, we analyze the EMF exposure level for the user holding the device. In the proximity of the UEs, high EMF exposure levels may come from the coherent combination of the signal, specially if channels have not been accurately estimated. In this case, an appropriate performance figure could be how fast does the RF power density falls as a spatial point moves away from the device antenna.

Using the derivations in previous section, the first-order statistics of the channel at a distance  $r_k$  from  $\text{UE}_k$ , and with angular position defined by  $0 \leq v_k \leq 2\pi$  (measured in the  $x-y$  plane) and  $0 \leq \omega_k \leq \pi$  (measured in the  $z$  axis), can be defined as  $\bar{\mathbf{h}}_{kn}(v_k, \omega_k, r_k)$  in a similar way to (35) but with a virtual measurement point located at

$$\zeta_k(v_k, \omega_k, r_k) = [x_k^{\text{ue}} + r_k \sin \omega_k \cos v_k, y_k^{\text{ue}} + r_k \sin \omega_k \sin v_k, z_k^{\text{ue}} + r_k \cos \omega_k]. \quad (42)$$

This point lies in the  $r_k$ –radius sphere centered at  $\zeta_k^{\text{ue}}$  as illustrated in Fig. 3. Then, the expected RF power density at a distance  $r_k$  from  $\text{UE}_k$ , herein called  $r_k$ –proximity region, is given by

$$P_{D,k}(r_k) = \frac{1}{4\pi r_k^2} \int_0^{2\pi} \int_0^\pi \text{Tr}(\mathbf{V}^T \bar{\mathbf{H}}_k(v_k, \omega_k, r_k)) d\omega_k dv_k = \frac{1}{4\pi r_k^2} \text{Tr}(\mathbf{V}^T \bar{\mathbf{H}}_k^f(r_k)) [\text{W/m}^2], \quad (43)$$

where  $\bar{\mathbf{H}}_k^f(r_k) = \int_0^{2\pi} \int_0^\pi \bar{\mathbf{H}}_k(v_k, \omega_k, r_k) d\omega_k dv_k$ ,  $\bar{\mathbf{H}}_k(v_k, \omega_k, r_k) = \bar{\mathbf{h}}_k(v_k, \omega_k, r_k) \bar{\mathbf{h}}_k(v_k, \omega_k, r_k)^H$  and

$$\bar{\mathbf{h}}_k(v_k, \omega_k, r_k) = [\bar{\mathbf{h}}_{k1}(v_k, \omega_k, r_k)^T, \bar{\mathbf{h}}_{k2}(v_k, \omega_k, r_k)^T, \dots, \bar{\mathbf{h}}_{kN}(v_k, \omega_k, r_k)^T]^T. \quad (44)$$

Thus,  $\bar{\mathbf{H}}_k^f(r_k) \succeq 0$ ,  $\forall k$ . Note that this requires using (35) but with  $\zeta_k(v_k, \omega_k, r_k)$  instead of  $\zeta_k^{\text{ue}}$ .

Using (43), the RF power density falls with a rate of

$$\partial P_{D,k}(r_k) = \frac{1}{4\pi r_k^2} \left( \text{Tr}(\mathbf{V}^T \partial \bar{\mathbf{H}}_k^f(r_k)) - \frac{2}{r_k} \text{Tr}(\mathbf{V}^T \bar{\mathbf{H}}_k^f(r_k)) \right). \quad (45)$$

However, current regulations and EMF-related constraints are more compatible with  $P_{D,k}(r_k)$  rather than with  $\partial P_{D,k}(r_k)$ . Thus, we adopt EMF constraints of the form

$$P_{D,k}(r_0) \leq \Theta_1, \quad \forall k, \quad (46)$$

for a certain measurement distance  $r_0 > 0$  of interest. Then, (46) can be easily incorporated to the SDP and low-complexity optimization frameworks in Sections III and IV, respectively.

### C. EMF Exposure Level for a Random Human

Herein, we set system constraints to prevent high EMF exposure to any random human (and living species), not necessarily associated to (in the proximity of) the served UEs. Note that the RF LOS receive power at a virtual measurement point  $\zeta = [x, y, z]$  is given by

$$P(x, y, z) = \text{Tr}(\mathbf{V}^T \bar{\mathbf{H}}(x, y, z)), \quad (47)$$

where  $\bar{\mathbf{H}}(x, y, z) = \bar{\mathbf{h}}(x, y, z) \bar{\mathbf{h}}(x, y, z)^H$  with

$$\bar{\mathbf{h}}(x, y, z) = [\bar{\mathbf{h}}_{k1}(x, y, z)^T, \bar{\mathbf{h}}_{k2}(x, y, z)^T, \dots, \bar{\mathbf{h}}_{kN}(x, y, z)^T]^T, \quad (48)$$

which requires using (35) but with  $\zeta$  instead of  $\zeta_k^{\text{ue}}$ . Ideally, one would like to have a constraint of the kind  $P(x, y, z) \leq \Theta_2$ ,  $\forall x, y, z$  out of the  $r_k$ –proximity region of each  $\text{UE}_k$ , where  $\Theta_2$  is the allowed RF power exposition level. However, this would require imposing an infinite number of constraints since the number of triplets  $[x, y, z]$  is infinite, and even a discretization of the volumetric space may not be advisable as some critical points may be left out. Instead, we adopt

a probabilistic constraint as

$$\mathbb{P}[P(x, y, z) \geq \Theta_2] \leq \varepsilon, \quad (49)$$

where  $\varepsilon \ll 1$  is a tolerable violation probability<sup>6</sup>, and  $x, y, z$  are uniformly distributed random variables in the region of interest. This kind of constraint is in general difficult to address since the distribution of  $P(x, y, z)$  depends on the system configuration parameters, thus, herein we transform it into an average constraint by using Markov inequality, thus, further constraining the feasibility solution set, as

$$\mathbb{P}[P(x, y, z) \geq \Theta_2] \leq \mathbb{E}[P(x, y, z)]/\Theta_2 \leq \varepsilon \rightarrow \mathbb{E}[P(x, y, z)] \leq \varepsilon\Theta_2. \quad (50)$$

To proceed further, we distinguish two main regions as illustrated in Fig. 4:

- $R_0$  : proximity to the radio stripes, so that the probability of human (living) tissue goes to 0,
- $R_1$  : remaining deployment area where humans (and living species) can freely and safely be, excluding all the  $r_k$ -proximity regions.

We focus our discussions on  $R_1$ , which is critical. However we would like to place some comments regarding  $R_0$ , which may be a region with non-controlled or partially controlled EMF exposure levels. In case of the former, a manual switch-off mechanism may be needed if a human enters the region. Meanwhile, in case of the latter, sensing mechanisms may be deployed to detect the human presence and switch-off the system, or alternative force the system to comply with the EMF regulations also in that region. Thus, in addition to aforementioned power density and RF power exposure constraint, the system may need to comply with additional regulations when a human is sensed in  $R_0$ , e.g., specific absorption rate (SAR) constraints<sup>7</sup>.

Regarding the region of interest,  $R_1$ , we can proceed as follows

$$\mathbb{E}[P(x, y, z)] = \frac{\Omega_0 - \sum_{k=1}^K \Omega_k}{V_0 - \sum_{k=1}^K V_k}, \quad (51)$$

where  $\Omega_0$  corresponds to the sum RF power in the complete region  $R_1$ , thus, with volume  $V_0 = (G - G')L^2/16$  according to Fig. 4, and  $\Omega_k$  corresponds to the sum RF power in the sphere defined by the  $r_k$ -proximity region, thus with volume  $V_k = 4\pi r_k^3/3$ . Notice that

<sup>6</sup>EMF-related stochastic constraints may be unavoidable in practical systems because of the randomness triggered by many known and unknown factors [35]. In the context of WET, authors in [23] even propose the notion of probabilistic EMF safety that requires the probability that EMF intensity anywhere does not exceed a given threshold with a given strict confidence.

<sup>7</sup>SAR measures the absorbed power from fields between 100 kHz and 10 GHz in a unit mass of human tissue by using units of [W/kg], and dominates the RF exposure for very short distances (e.g., less than few tens of centimeters) [36], [37].

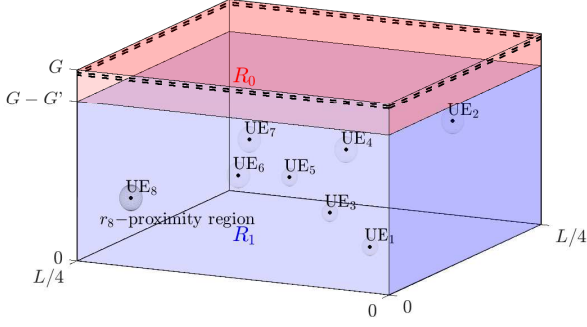


Fig. 4. Main operation regions. For illustration purposes, the position of the EH devices are set as  $\zeta_k^{\text{ue}} = [Lk/32, Lk/32, 2^{k/7-1}]$  for odd  $k$ , while  $\zeta_k^{\text{ue}} = [L(9-k)/32, Lk/36, 2^{1-k/7}]$  for even  $k$ , with  $K = 8$ .

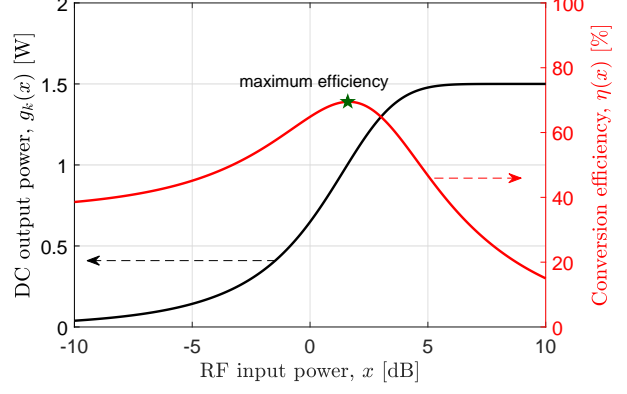


Fig. 5. EH transfer function and conversion efficiency for  $a = 2$ ,  $b = 1$  and  $\nu_k = 1.5$  W.

$$\Omega_0 = \int_0^{G-G'} \int_0^{L/4} \int_0^{L/4} P(x, y, z) dx dy dz = \text{Tr}(\mathbf{V}^T \bar{\mathbf{H}}), \quad (52)$$

$$\Omega_k = \int_0^{r_k} \text{Tr}(\mathbf{V}^T \bar{\mathbf{H}}_k(r)) dr = \text{Tr}(\mathbf{V}^T \bar{\mathbf{H}}_k), \quad (53)$$

which comes from using  $\bar{\mathbf{H}}_k = \int_0^{r_k} \bar{\mathbf{H}}_k^f(r) dr$ , where  $\bar{\mathbf{H}}_k^f(r)$  is defined after (43), and from using  $P(x, y, z)$  given in (47) and setting  $\bar{\mathbf{H}} = \int_0^{G-G'} \int_0^{L/4} \int_0^{L/4} \bar{\mathbf{H}}(x, y, z) dx dy dz$ . By substituting (52) and (53) into (51), (50) can be rewritten as

$$\text{Tr}(\mathbf{V}^T \mathbf{H}_{\text{eff}}) \leq \varepsilon \left( V_0 - \sum_{k=1}^K V_k \right) \Theta_2 \triangleq \bar{\Theta}_2, \quad (54)$$

where  $\mathbf{H}_{\text{eff}} = \bar{\mathbf{H}} - \sum_{k=1}^K \bar{\mathbf{H}}_k$ . Then, (54) can be immediately incorporated to the SDP and MRT-based optimization frameworks in Sections III and IV-B, respectively. However, observe that  $\mathbf{H}_{\text{eff}}$  may not be positive semi-definite, thus

$$\text{Tr}(\mathbf{V}^T \mathbf{H}_{\text{eff}}) = \sum_{k=1}^K \mathbf{v}_k^H \mathbf{H}_{\text{eff}} \mathbf{v}_k \leq \bar{\Theta}_2 \quad (55)$$

is not guaranteed to impose a convex constraint on  $\{\mathbf{v}_k\}$ , and cannot be incorporated directly to the SCA-based precoding designed in Section IV-A, and specifically given in Algorithm 3. Therefore, we compute the eigendecomposition of  $\mathbf{H}_{\text{eff}}$ , which allows us to write  $\mathbf{H}_{\text{eff}} = \mathbf{H}_{\text{eff},1} + \mathbf{H}_{\text{eff},2}$ , where  $\mathbf{H}_{\text{eff},1} \succeq 0$  and  $\mathbf{H}_{\text{eff},2} \prec 0$  are the matrices associated with the positive/negative eigenvectors of  $\mathbf{H}_{\text{eff}}$ , respectively. Since now  $\text{Tr}(\mathbf{V}^T \mathbf{H}_{\text{eff}}) = \text{Tr}(\mathbf{V}^T \mathbf{H}_{\text{eff},1}) + \text{Tr}(\mathbf{V}^T \mathbf{H}_{\text{eff},2})$  is the sum of a convex and concave function, one can easily apply the SCA technique here. Specifically, the linearization is applied to the (concave) second term, thus, similar to (16), the

additional iterative constraint to be included in **P3** is given by

$$\text{Tr}(\mathbf{V}^T \mathbf{H}_{\text{eff},1}) + 2 \sum_{k=1}^K \Re\{\bar{\mathbf{v}}_k^H \mathbf{H}_{\text{eff},2}^T \mathbf{v}_k\} - \text{Tr}(\bar{\mathbf{V}}^T \mathbf{H}_{\text{eff},2}) \leq \bar{\Theta}_2. \quad (56)$$

Finally, note that because of the use of Markov inequality in the derivations, the violation probability of  $P(x, y, z) \leq \Theta_2$  is in fact smaller than  $\varepsilon$ , but cannot be established beforehand.

## VII. NUMERICAL RESULTS

In this section, we illustrate the performance of discussed radio stripes system for WET with/without the introduced EMF-related constraints.

### A. Configuration setup

Unless stated otherwise we set the system parameters as given next.

*a) Scenario Geometry:* We consider a room with dimensions  $6 \times 6 \times 3$  m<sup>3</sup>, where the radio stripes system is assumed at the ceiling level, i.e.,  $z^{\text{ap}} = G = 3$  m. Moreover, we set  $G' = 2.5$  m, and unless stated otherwise,  $f = 4$  GHz is the central operation frequency, for which  $\lambda = 7.5$  cm. The minimum separation constraint between consecutive PBs is set to  $l_0 = 10$  cm.

*b) Transmit/Receive/Channel Parameters:* PBs are equipped with  $M = 8$  antennas. Moreover, UEs transmit the pilot symbols with  $p_k = 10$  mW at each coherence time interval, while PBs' receive circuits experience an AWGN noise with  $\sigma^2 = -100$  dBm. Channels remain static for  $\tau = 1000$  channel uses, and  $\tau_p = K$ . UEs' EH requirements are assumed homogeneous and equal to 1 W (power and energy are equivalent by assuming normalized block time). Additionally, the spatial correlation matrices  $\{\mathbf{R}_{kn}\}$  are generated using the Gaussian local scattering model [32, Cap. 2] with angular standard deviation of  $10^\circ$ .

*c) EH Transfer Function:* We consider the following EH transfer function [38]:

$$g_k(x) = \nu_k \left( \frac{1 + e^{ab}}{1 + e^{-a(x-b)}} - 1 \right) e^{-ab}, \quad \forall x \geq 0, \quad (57)$$

which is known to describe accurately the nonlinearity of EH circuits by properly fitting parameters  $a, b \in \mathbb{R}^+$ . Note that (57) does not model the sensitivity ( $\omega_k$ ) phenomenon since  $g(x) = 0$  only when  $x = 0$ . However, the region of  $x \rightarrow g^{-1}(\omega_k)$  in (57) is of little interest in practice since the EH capabilities there are very limited, specially in the scenario under discussion here where devices are power-hungry. Finally, the conversion efficiency is given by  $\eta(x) = g(x)/x \in [0, 1]$ . Fig. 5 illustrates the EH transfer function and conversion efficiency when  $a = 1$ ,  $b = 4$  and  $\nu_k = 4$  W. We use these parameter values, which do not correspond to any specific EH circuit

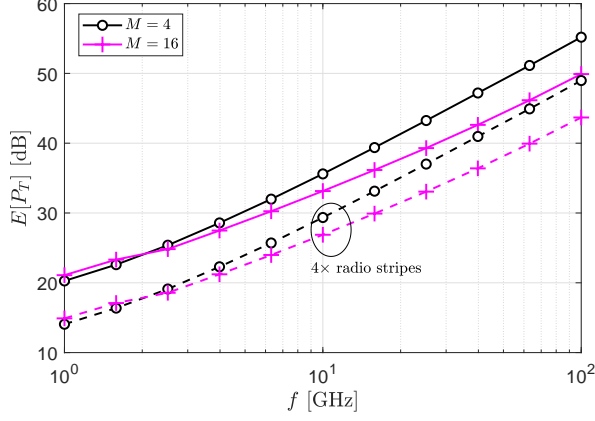


Fig. 6. Average total transmit power as a function of  $f$  for  $M \in \{4, 16\}$ . The dashed curves represent the system performance when the radio stripes system is four-fold vertically replicated with inter-stripes separation distance  $l_0$ .

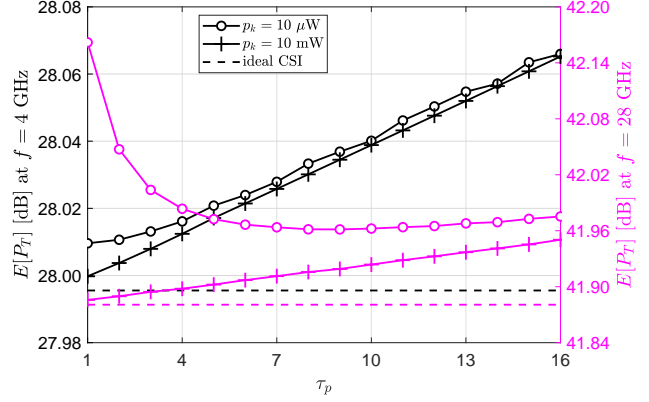


Fig. 7. Average total transmit power as a function of the number of training pilots for  $f \in \{4, 28\}$  GHz.

implementation, for illustration purposes. The reasons are that EH circuits prototyping for high-power rectifying, e.g., [39]–[42], are less common than for low-power implementations, which makes difficult selecting an appropriate circuit for a broad range of RF power inputs. Moreover, circuits are designed for a specific frequency range, while we will be exploring the system performance for different frequency ranges, which would require different EH circuit designs to keep approximately the same EH transfer function. Back to Fig. 5, observe the maximum conversion efficiency peak at 7.4 dB (5.5 W) for which  $\eta = 59\%$ . Since energy requirements per transmit block are fixed, i.e.,  $\{\xi_k\}$  is given, the optimum system efficiency (min  $P_T$ ) is attained when all devices are operating at such point.

### B. Unconstrained Optimization - Single UE

Herein, we focus on the performance of the system when serving a single UE at a critical position, i.e.,  $\zeta^{\text{ue}} = [3, 3, 0]^T$ , which is the point that is simultaneously farthest from all the PBs. We omit the per-PB power and EMF-related constraints, thus, the MRT-based precoding specified in (22) with  $p = \delta_1 / \|\hat{\mathbf{h}}_1\|^2$  is the optimum, thus it is used throughout this subsection.

Fig. 6 shows the average transmit power requirements to serve the UE as a function of the operation frequency. For each frequency, it is assumed that the radio stripes system is composed of the maximum allowed number of PBs, which matches (34). Observe that as the frequency increases, the spatial transmit gains increase as well since more PBs/antennas can be incorporated to the radio stripes system. However, such gains do not compensate the path loss, which grows following a power-law with exponent  $2 - 2.49$  according to (36) and (38). Moreover, note that

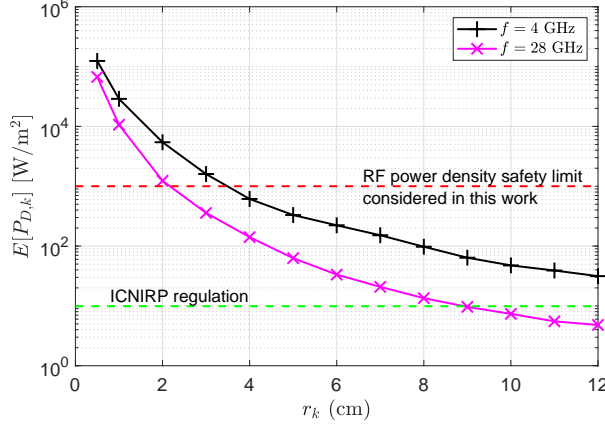


Fig. 8. RF power density as a function of  $r_k$  for  $f \in \{4, 28\}$  GHz.

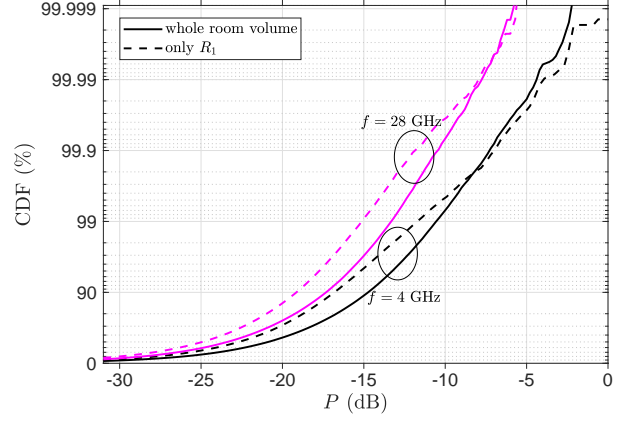


Fig. 9. CDF of the RF power exposure in the room for  $f \in \{4, 28\}$  GHz.

equipping each PB with more antennas becomes more attractive than increasing the number of PBs as the frequency increases. This is because such strategy allows obtaining a greater value of  $MN$  (given the scenario geometry and inter-PB separation constraints, see (34)), which, rather than the individual contributions from  $M$  and  $N$ , determines the system performance when operating without per-PB power and EMF-related constraints. It becomes evident that additional boosting performance strategies are needed to increase the overall system efficiency, and make the technology viable in practice. For instance, by increasing  $l$ -fold the number of transmit antennas, the system power consumption is approximately reduced  $l$ -fold as well, as illustrated in the figure for  $l = 4$ .

Fig. 7 illustrates the average transmit power consumption as a function of the duration of the CSI acquisition phase for  $f \in \{4, 28\}$  GHz. There is a trade-off here: the smaller  $\tau_p$  is, the worse the CSI estimate becomes, however as  $\tau_p$  increases, less time is left for WET; thus, both a too small or too large  $\tau_p$  may affect the system efficiency. In the figure, this is most evident for  $f = 28$  GHz and  $p_k = 10 \mu\text{W}$ , for which  $\tau_p^{\text{opt}} = 9$ , since  $\tau_p^{\text{opt}} = 1$  for other configurations. Even when training power is critically reduced, e.g., to  $10 \mu\text{W}$ , the system performance does not worsen significantly, which supports our prior claims around (2). In a nutshell, training is not a critical (limiting) factor for this system as just little energy is required to attain a performance similar to that of a system with ideal CSI, thus, training operation configured with small number of pilots (the minimum possible, i.e.,  $\tau_p = K$ ) and small transmit power seems advisable.

Figs. 8 and 9 show the performance in terms of EMF exposure. Although for higher frequency transmit power increases for the same target EH requirement at the UE to compensate the frequency-dependent losses (as shown in Figs. 6 and 7), the system becomes more EMF friendly.



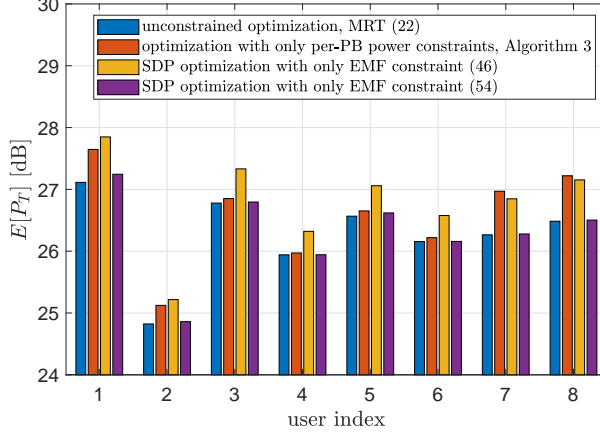


Fig. 10. Average total transmit power when serving a single UE at the positions in Fig. 4. We compare the performance of the optimal i) unconstrained optimization, given by the MRT precoder in (22), ii) optimization with only the per-PB power constraints, given in Algorithm 3, iii) SDP optimization with only the EMF constraint in (46), and iv) SDP optimization with only the EMF constraint in (54).

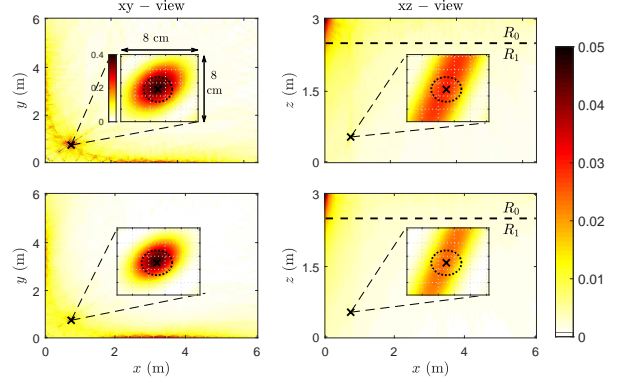


Fig. 11. Heatmap of the RF power (averaged over the missing axis, e.g., averaged over the  $z$ -axis when presented in the  $xy$ -view) in the room when powering UE<sub>1</sub>. We set  $p_{\max} = 17$  dB, and show the system performance when operating without (first-row plots) and with (second-row plots) EMF-related constraints. The plots corresponding to the  $yz$ -view are not shown as they coincide the ones for the  $xz$ -view since  $x$  and  $y$  coordinates of UE<sub>1</sub> match.

This is because of the better spatial resolution, i.e., smaller wavelength ( $\lambda = 1.07$  cm at 28 GHz). Specifically, Fig. 8 illustrates the average RF power density in the  $r_k$ -proximity of the UE for  $f \in \{4, 28\}$  GHz. As observed, the MRT-based precoding alone (without EMF-related constraints) guarantees that the RF power density at distances larger than 2 cm from the UE is below  $1000 \text{ W/m}^2$  at 28 GHz.<sup>8</sup> Fig. 9 displays the cumulative distribution function (CDF) of the RF power exposure in the room, i.e.,  $P(x, y, z)$  in (47). Herein we observe that the chances of high RF power exposure, e.g.,  $\sim 1 \text{ W}$ , at a certain spatial point in  $R_1$  are significantly small.

### C. Constrained Optimization

Herein, we consider a single UE at different locations (Fig. 10 and Fig. 11), or multiple UEs (Fig. 12 and Fig. 13). We consider eight different locations for the UEs as illustrated in Fig. 4. Unless stated otherwise, we set  $p_{\max} = 10$  dB and the parameters related to the EMF radiation constraints as  $r_k = 1.5$  cm,  $\Theta_1 = 1000 \text{ W/m}^2$  [21],  $\varepsilon = 10^{-2}$  and  $\Theta_2 = 0.25 \text{ W}$ .

1) *Single UE at Multiple Locations*: Fig. 10 shows the system's average transmit power when serving a single UE at different positions. Note that the UE location significantly affects the system performance. For instance, the radio stripes system may need just 25 dB to serve

<sup>8</sup>Current regulations impose much more stringent EMF radiation constraints. For instance, ICNIRP establishes the power density safety threshold at  $\sim 9.9 \text{ W/m}^2$  (61 V/m) [43], which has been depicted in Fig. 8 as well. Even so, we adopt  $\Theta_1 = 1000 \text{ W/m}^2$ , above which there might be skin affectations [21], for our discussions in the next subsection since using smaller values would demand operating at higher frequencies, which is extremely computationally demanding and thus requires further and dedicated research. Please refer to our specific discussions on this in Section VIII.

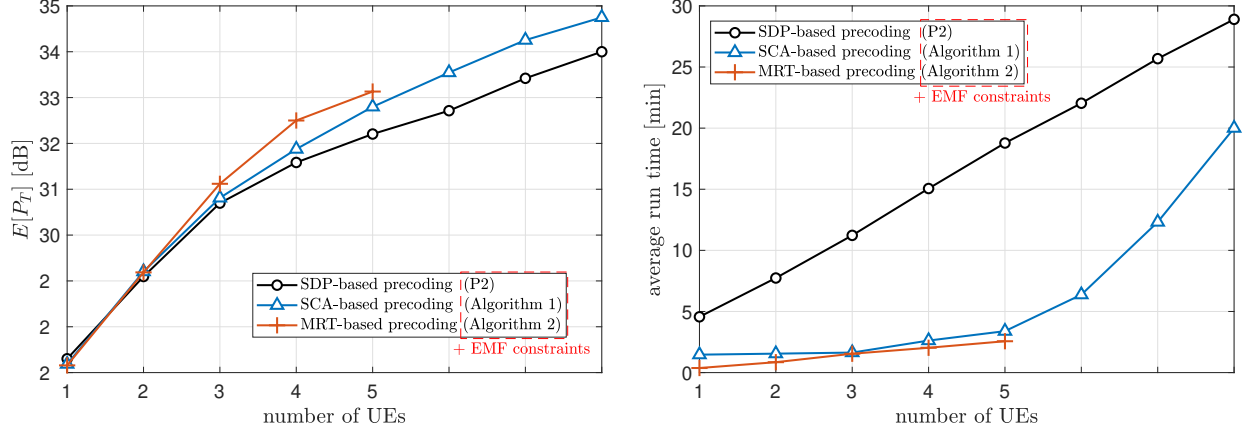


Fig. 12. a) Average total transmit power (left) and b) average optimization run time (right) as a function of the number of UEs.  $UE_2$ , while the value scales up to 27 – 28 dB when serving  $UE_1$ . Moreover, the system incurs in a greater transmit power consumption once the per-PB power and EMF-related constraints are considered. Specifically, the per-PB power constraint affects more critically the system performance when serving  $UE_1$ ,  $UE_2$ ,  $UE_7$  and  $UE_8$ , which are closer to the radio stripes as illustrated in Fig. 4. Observe also that the EMF constraint for the proximity region of the UE is often active, thus, critically influencing the system performance by demanding an increased radio stripes' transmit power to safely diffuse the energy around a UE, while the EMF constraint for  $R_1$  is not leading to a significant performance degradation of the system.

In Fig. 11, a heatmap of the RF power in the room is shown when powering only  $UE_1$ . We relaxed the per-PB power constraint to  $p_{\max} = 17$  dB such that the main performance affectations come from the EMF-related constraints. The EMF-aware precoding somewhat homogenizes the RF radiation over the region  $R_1$  compared to the precoding without EMF-related constraints. Meanwhile, the RF power density in the proximity of the UE becomes a bit less intense but more homogeneous around the center to meet the corresponding EMF constraint.

2) *Multiple UEs*: In the remaining figures, we evaluate the performance in terms of average transmit power consumption and average required tun time as a function of the number of UEs. Powering  $k$  UEs means powering  $UE_1, \dots, UE_k$  with positions illustrated in Fig. 4. As a multi-UE system is now considered, we relax some system constraints to favor optimization feasibility, i.e.,  $r_k = 2$  cm, and  $p_{\max} = 20$  dB. The three key optimization frameworks, say i) SDP-based precoding (P2), ii) SCA-based precoding (Algorithm 1), and iii) MRT-based precoding (Algorithm 2), are evaluated subject to EMF constraints using CVX [26].

Fig. 12 evinces that the SDP-based framework leads to the most efficient transmit power

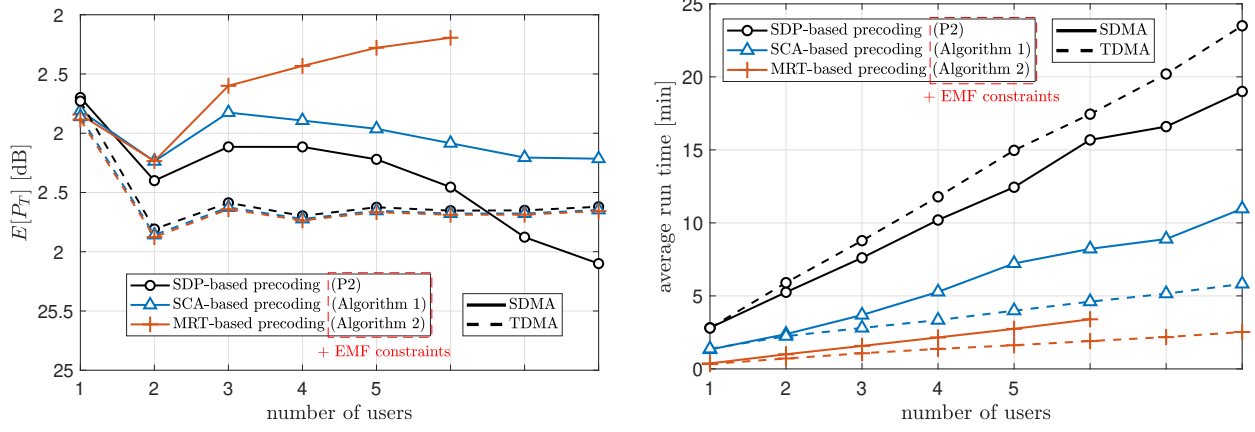


Fig. 13. TDMA vs SDMA in terms of a) average total transmit power (top) and b) average optimization run time (bottom) when serving an increasing number of UEs. We set  $\xi = 1/k$  so the total harvested power remains at 1 W independently of the number of users.

consumption, however is extremely costly and the complexity increases linearly with the number of UEs. The SCA-based framework should have led to the global optimum solution, however this was not the case when serving 3 or more UEs since we stopped the SCA iterative procedure before reaching accurate convergence as the solver run into numerical approximation errors.<sup>9</sup> The MRT-based framework performs extremely well when serving a small number of UEs. However, in the considered setup, serving five or more UEs is not possible when using such framework due to unfeasibility, i.e., the power domain tuning is insufficient for handling the EMF-related constraints. In such cases, the degrees of freedom related to the beamformer phase shift optimization (as used in the SDP- and SCA-based framework) are critically required.

In case of multi-UE scenarios, we aimed so far at powering all the UEs simultaneously by exploiting SDMA. Alternatively, the radio stripes system may exploit a TDMA technique, under which a single UE is powered at the time. However, TDMA may be infeasible for powering any number  $K$  of UEs, with a given set of energy demands  $\{\xi_k\}$ , as the power required to be harvested at each  $UE_k$  increases  $K$  times (since charging time reduces in the same proportion), and the EH circuit may not support it, i.e.,  $K\xi_k > \nu_k$ . Anyways, let us force feasibility by setting  $\xi_k = 1/K$  so the total harvested power remains at 1 W independently of the number of users, and compare TDMA vs SDMA as shown in Fig. 13. Observe that there is not functioning distinction between TDMA and SDMA for  $k = 1$ , thus their corresponding performances match. Again,  $UE_1$  is shown to be costly to serve, specially compared to  $UE_2$ . Moreover, TDMA is shown to

<sup>9</sup>This issues comes from running a convex optimization tool as CVX inside an ‘outer’ independent loop. In practice, an integrated KKT-based SCA optimization solver would not have faced this issue and would lead to the global optimum.

be the most efficient in terms of average transmit power consumption when serving a relatively small number of UEs. This is mainly because, independently of the number of UEs, the EH circuit efficiency is kept high as its output is fixed at 1 W, while the output is proportionally reduced as the number of devices increases when using SDMA. Meanwhile, when the number of UEs is significantly large such lower RF incident power requirement at each UE makes easier satisfying the EMF-related constraints, thus SDMA may outperform TDMA. In terms of complexity, TDMA is shown to be more computationally costly than SDMA when using the global optimum SDP-based framework, while the opposite occurs when using SCA/MRT-based precoding. However, notice that using SDMA requires a costly single-shot optimization, while the TDMA optimization may be allowed to expand over the entire block coherence time as it is composed of a series of  $k$  successive less-complex optimization processes, thus, it may be more flexible for implementation. Moreover, TDMA allows using performance and cost efficient SCA- and even MRT-based frameworks, which work well for serving a single UE at the time. In general, the performance trade-offs between SDMA and TDMA are strictly dominated by the EH non-linearity and the EMF-related constraints, and further study is needed.

## VIII. CONCLUSION AND FUTURE WORKS

We introduced an indoor cell-free mMIMO system with radio stripes for wirelessly charging power-hungry UEs. We derived optimal and sub-optimal precoders based on SDP, SCA and MRT that aim to minimize the radio stripes' transmit power subject to stringent EH requirements per UE, while exploiting CSI and information of the PTE of the EH circuits. MRT/SCA-based precoders resulted to be particularly appealing when serving a small number of UEs. Additionally, we proposed an analytical framework to assess the EMF radiation exposure. We focused on the RF power density in the proximity of the UEs, and the RF power caused at a random point. These figures were incorporated as EMF-related constraints to the precoding optimization problems, thus making the WET precoding safe. Numerical results showed that the EMF radiation exposure can be more easily controlled at higher frequencies at the cost of a higher transmit power consumption. Moreover, we verified that training is not a limiting factor for the considered indoor system as just little energy is required to attain a performance similar to that of ideal CSI. We discussed key trade-offs between SDMA and TDMA scheduling. TDMA is the most efficient choice in terms of average transmit power consumption when serving a relatively small

number of UEs, while SDMA may be preferable when the number of UEs is relatively large. Some interesting research directions that we may pursue in future work are given next:

1) *Computationally affordable methods for higher frequencies:* The high operation frequency (needed to enable safe WET) makes simulations extremely costly. As the operation frequency increases, the LOS channel becomes more oscillatory in space, thus, making rather challenging to efficiently perform the numeric integration in (43), (52) and (53), even on high-tech computing servers available nowadays, taking weeks to finalize. In this work, we focused on the 4 GHz operation and thus adopted a relatively high power density threshold, i.e.,  $\Theta_1 = 1000 \text{ W/m}^2$  (even when current regulations impose much more stringent constraints, e.g.,  $\sim 9.9 \text{ W/m}^2$  (61 V/m) [43]) to enable feasibility. As operation at higher frequencies may be a must, future research can focus on addressing above issues, e.g., by using principal component analysis to reduce the dimensionality of the data sets without seriously compromising accuracy [44].

2) *Reduce energy waste:* As evinced in Section VII, the efficiency of the considered system is considerably low, usually in the range of 0.1%–1%, which means that 99%–99.9% of the energy is wasted mainly due to distance/frequency/hardware-dependent losses. To make technology profitable and enable sustainability, such energy waste must be reduced as much as possible. In Fig. 6, we showed the significant performance gains from increasing the number of transmit antennas, but even greater gains may be reachable by increasing the number receive antennas per UE. For instance, say the EH hardware is constrained on a dimension of  $4 \text{ cm} \times 4 \text{ cm}$ , then, operating at 4 GHz, 28 GHz, 100 GHz, allows equipping the UEs with up to 4, 71, 765 half-wavelength spaced EH antennas, respectively. Since problem dimensions would increase, it may be better exploring affordable computing methods beforehand, as highlighted above. Moreover, observe that there might be an increased energy waste when serving multiple users simultaneously, specially because the EMF-related constraints become more difficult to meet, thus intelligent scheduling mechanisms are worth investigating.

3) *Impact of outdated/quantized CSI and radio stripes processing:* Channel training was shown to be not critical for the considered quasi-static indoor scenario. However, the assumption of quasi-static fading is ideal per se, thus it would be interesting to evaluate a potential performance degradation due to outdated CSI. Moreover, since the considered system performs centralized optimization/decisions, each PB needs to inform the estimated CSI to the CPU over limited-capacity front-haul connections. The performance losses due to quantized CSI and energy beamformers may be significant and worth evaluating. Novel sequential [45] or parallel [46]

processing methods together with worst case noise designs may be attractive here.

## REFERENCES

- [1] O. L. A. López *et al.*, “Massive wireless energy transfer: Enabling sustainable IoT toward 6G era,” *IEEE Internet Things J.*, vol. 8, no. 11, pp. 8816–8835, 2021.
- [2] N. H. Mahmood *et al.*, “White paper on critical and massive machine type communication towards 6G,” *6G Research Visions*, no. 11, 2020, <http://jultika.oulu.fi/files/isbn9789526226781.pdf>.
- [3] K. Huang and X. Zhou, “Cutting the last wires for mobile communications by microwave power transfer,” *IEEE Commun. Mag.*, vol. 53, no. 6, pp. 86–93, 2015.
- [4] B. Clerckx *et al.*, “Wireless power transfer for future networks: Signal processing, machine learning, computing, and sensing,” *arXiv:2101.04810*, 2021.
- [5] B. Clerckx and E. Bayguzina, “Waveform design for wireless power transfer,” *IEEE Trans. Signal Process.*, vol. 64, no. 23, pp. 6313–6328, 2016.
- [6] O. L. A. López *et al.*, “On CSI-free multi-antenna schemes for massive wireless energy transfer,” *IEEE Internet Things J.*, pp. 1–1, 2020.
- [7] O. L. A. López *et al.*, “A low-complexity beamforming design for multiuser wireless energy transfer,” *IEEE Wireless Commun. Lett.*, vol. 10, no. 1, pp. 58–62, 2021.
- [8] O. M. Rosabal *et al.*, “On the optimal deployment of power beacons for massive wireless energy transfer,” *IEEE Internet Things J.*, pp. 1–1, 2020.
- [9] S. D. Van *et al.*, “Wireless powered wearables using distributed massive MIMO,” *IEEE Trans. Commun.*, vol. 68, no. 4, pp. 2156–2172, 2020.
- [10] G. Yang *et al.*, “Throughput optimization for massive MIMO systems powered by wireless energy transfer,” *IEEE J. Sel. Areas Commun.*, vol. 33, no. 8, pp. 1640–1650, 2015.
- [11] T. Khan *et al.*, “Optimization of power transfer efficiency and energy efficiency for wireless-powered systems with massive MIMO,” *IEEE Trans. Wireless Commun.*, vol. 17, no. 11, pp. 7159–7172, 2018.
- [12] S. Lee *et al.*, “Retrodirective multi-user wireless power transfer with massive MIMO,” *IEEE Wireless Commun. Lett.*, vol. 7, no. 1, pp. 54–57, 2018.
- [13] J. Wang *et al.*, “Wireless energy transfer in extra-large massive MIMO Rician channels,” *IEEE Trans. Wireless Commun.*, pp. 1–1, 2021.
- [14] F. Zhu *et al.*, “Robust simultaneous wireless information and power transfer in beamspace massive MIMO,” *IEEE Trans. Wireless Commun.*, vol. 18, no. 9, pp. 4199–4212, 2019.
- [15] L. Zhao and X. Wang, “Massive MIMO downlink for wireless information and energy transfer with energy harvesting receivers,” *IEEE Trans. Commun.*, vol. 67, no. 5, pp. 3309–3322, 2019.
- [16] C. F. Pan *et al.*, “Intelligent reflecting surface aided MIMO broadcasting for simultaneous wireless information and power transfer,” *IEEE J. Sel. Areas Commun.*, vol. 38, no. 8, pp. 1719–1734, 2020.
- [17] Q. Zhang *et al.*, “Mobile crowd wireless charging toward rechargeable sensors for Internet of Things,” *IEEE Internet Things J.*, vol. 5, no. 6, pp. 5337–5347, 2018.
- [18] J. Xu *et al.*, “UAV-enabled wireless power transfer: Trajectory design and energy optimization,” *IEEE Trans. Wireless Commun.*, vol. 17, no. 8, pp. 5092–5106, 2018.
- [19] G. Interdonato *et al.*, “Ubiquitous cell-free massive MIMO communications,” *J. Wirel. Commun. Netw.*, vol. 2019, no. 1.

- [20] A. Ahlbom *et al.*, “Guidelines for limiting exposure to time-varying electric, magnetic, and electromagnetic fields (up to 300 GHz),” *Health Phys.*, vol. 74, no. 4, pp. 494–521, 1998.
- [21] L.-G. Tran *et al.*, “RF power harvesting: a review on designing methodologies and applications,” *Micro Nano Syst. Lett.*, vol. 5, no. 1, pp. 1–16, 2017.
- [22] H. Dai *et al.*, “Safe charging for wireless power transfer,” *IEEE/ACM Trans. Netw.*, vol. 25, no. 6, pp. 3531–3544, 2017.
- [23] R. Dai *et al.*, “Robustly safe charging for wireless power transfer,” in *IEEE INFOCOM*, 2018, pp. 378–386.
- [24] O. Özdogan *et al.*, “Massive MIMO with spatially correlated Rician fading channels,” *IEEE Trans. Commun.*, vol. 67, no. 5, pp. 3234–3250, 2019.
- [25] B. Clerckx and J. Kim, “On the beneficial roles of fading and transmit diversity in wireless power transfer with nonlinear energy harvesting,” *IEEE Trans. Wireless Commun.*, vol. 17, no. 11, pp. 7731–7743, Nov. 2018.
- [26] M. Grant and S. Boyd, “CVX: Matlab software for disciplined convex programming,” <http://cvxr.com/cvx>, Mar. 2014.
- [27] N. Sidiropoulos *et al.*, “Transmit beamforming for physical-layer multicasting,” *IEEE Trans. Signal Process.*, vol. 54, no. 6, pp. 2239–2251, 2006.
- [28] Y. Ye, *Interior point algorithms: theory and analysis*. John Wiley & Sons, 2011, vol. 44.
- [29] B. R. Marks and G. P. Wright, “A general inner approximation algorithm for nonconvex mathematical programs,” *Oper. Res.*, vol. 26, no. 4, pp. 681–683, 1978.
- [30] D. Kumar *et al.*, “Blockage-aware reliable mmWave access via coordinated multi-point connectivity,” *IEEE Trans. Wireless Commun.*, pp. 1–1, 2021.
- [31] S. Boyd and L. Vandenberghe, *Convex optimization*. Cambridge university press, 2004.
- [32] E. Björnson *et al.*, “Massive MIMO networks: Spectral, energy, and hardware efficiency,” *Found. Trends Signal Process.*, vol. 11, no. 3-4, pp. 154–655, 2017.
- [33] 3GPP TR 38.901, *5G: Study on channel model for frequencies from 0.5 to 100 GHz (V14.3.0)*. [Online]. Available: [https://www.etsi.org/deliver/etsi\\_tr/138900\\_138999/138901/14.03.00\\_60/tr\\_138901v140300p.pdf](https://www.etsi.org/deliver/etsi_tr/138900_138999/138901/14.03.00_60/tr_138901v140300p.pdf)
- [34] J. R. Hampton, *Introduction to MIMO communications*. Cambridge Univ. Press, 2014.
- [35] J. Wiart, *Radio-frequency human exposure assessment: from deterministic to stochastic methods*. John Wiley & Sons, 2016.
- [36] B. M. Hochwald, D. J. Love, S. Yan, P. Fay, and J. Jin, “Incorporating specific absorption rate constraints into wireless signal design,” *IEEE Commun. Mag.*, vol. 52, no. 9, pp. 126–133, 2014.
- [37] J. Zhang *et al.*, “Specific absorption rate-aware beamforming in MISO downlink SWIPT systems,” *IEEE Trans. Commun.*, vol. 68, no. 2, pp. 1312–1326, 2020.
- [38] E. Boshkovska *et al.*, “Practical non-linear energy harvesting model and resource allocation for SWIPT systems,” *IEEE Commun. Lett.*, vol. 19, no. 12, pp. 2082–2085, 2015.
- [39] M. Roberg *et al.*, “High-efficiency harmonically terminated diode and transistor rectifiers,” *IEEE Trans. Microw. Theory Techn.*, vol. 60, no. 12, pp. 4043–4052, 2012.
- [40] M. Litchfield *et al.*, “High-efficiency X-band MMIC GaN power amplifiers operating as rectifiers,” in *IEEE MTT-S IMS*, 2014, pp. 1–4.
- [41] D. Wang *et al.*, “Design of a high efficiency rectifier with wide bandwidth and input power range based on the time reversal duality of power amplifier,” in *EuMC*, 2015, pp. 291–294.
- [42] S. Abbasian and T. Johnson, “High efficiency GaN HEMT synchronous rectifier with an octave bandwidth for wireless power applications,” in *IEEE MTT-S IMS*, 2016, pp. 1–4.
- [43] M. K. Alhasnawi *et al.*, “Spectral density constraints on wireless communication,” *Heliyon*, vol. 6, no. 5, p. e03979, 2020.

- [44] I. T. Jolliffe and J. Cadima, "Principal component analysis: a review and recent developments," *Philos. Trans. Royal Soc. A*, vol. 374, no. 2065, p. 20150202, 2016.
- [45] Z. Shaik *et al.*, "Cell-free massive MIMO with radio stripes and sequential uplink processing," in *IEEE ICC WS*, 2020, pp. 1–6.
- [46] Y. Ma *et al.*, "Efficient parallel schemes for cell-free massive MIMO using radio stripes," *arXiv:2012.11076*, 2020.